The Nonstationarity of the Summer East Atlantic Pattern and its tropical-extratropical Teleconnection

Bachelor Thesis

B. Sc. Physics of the Earth System:
Meteorology, Oceanography, Geophysics

**Christian-Albrechts-Universität zu Kiel
GEOMAR Helmholtz Center for Ocean Research**

Author:	Ole Rieke
Matriculation Number:	1036858
First Examiner:	Prof. Dr. Richard J. Greatbatch
Second Examiner:	Dr. Gereon Gollan

December 2018

The Nonstationarity of the Summer East Atlantic Pattern and its tropical-extratropical Teleconnection

Ole Rieke

Abstract

Over the last 40 years, the Summer East Atlantic pattern has been the second most dominant mode of interannual variability in summer season over the North Atlantic European region after the Summer North Atlantic Oscillation. Previous studies found that the pattern has high impact on precipitation and temperature in Europe, causing very hot summers in central Europe when in its positive state. The pattern was also found to be related to tropical forcing by diabatic heating anomalies in the tropical Pacific and Caribbean that might be associated with the developing El Niño, resulting in a certain amount of predictability of the pattern. The aim of this thesis was to investigate the pattern in a preindustrial control run of the Max-Planck-Institue Earth System Model with a length of 700 years. It was found that, although the results could be verified in general, the Summer East Atlantic pattern itself, but also its impact on European climate and its tropical forcing, are highly nonstationary over time. Evidence is provided that the latest 40 years rather represent the current state of the Earth System than a constant condition, suggesting that future developments of the pattern might be different. Based on the finding that the last 40 years represent the maximum of tropical forcing and impact of the Summer East Atlantic pattern that was found in the model run, a future decrease of both its influence and its tropical forcing can be expected. Further mechanisms and possible reasons for this lack of robustness are presented. Furthermore, the influence of anomalies in sea surface temperature that are already present in the preceding spring on the pattern is analysed suggesting that this relation is connected to the tropical forcing by diabatic heating.

The Nonstationarity of the Summer East Atlantic Pattern and its tropical-extratropical Teleconnection

Ole Rieke

Zusammenfassung

Vorangegangene Studien haben das Sommer-Ost-Atlantik-Muster als zweitwichtigste Mode interannualer Variabilität im nordatlantisch-europäischen Raum ausgemacht. Das Muster hat weitreichende Auswirkungen auf das Klima im europäischen Sommer, in seiner positiven Phase sorgt es für sehr hohe Temperaturen in Zentral- und Osteuropa sowie für veränderte Niederschlagsmuster. Vergangene Studien haben gezeigt, dass das Sommer-Ost-Atlantik-Muster von Anomalien der diabatischen Heizung im tropischen Pazifik und dem Karibikraum angetrieben wird, die mit konvektiven Niederschlagsanomalien in diesen Regionen verknüpft sind. Ziel dieser Arbeit ist es, das Muster und diese Verbindung zu den Tropen in einem 700 Jahre umfassenden Modelllauf des Max-Planck-Institut Earth System Model zu untersuchen. Da sich der Modelllauf auf interne Variabilität konzentriert, ist der Einfluss von Treibhausgasen auf vorindustriellem Niveau festgesetzt. Obwohl die Ergebnisse vorheriger Studien grundsätzlich bestätigt werden konnten, wurde in der Analyse deutlich, dass das Muster selbst, aber besonders auch sein Einfluss auf das europäische Klima und der Antrieb aus den Tropen starken Schwankungen unterliegt. Dabei scheinen die vergangenen 40 Jahre einen Zeitraum aus dem Modelllauf zu repräsentieren, der sich durch maximale Dominanz und maximalen tropischen Antrieb des Musters auszeichnet. Das lässt vermuten, dass zukünftige Entwicklungen eher zu einer Reduktion dieses Antriebs und der Relevanz des Sommer-Ost-Atlantik-Musters für das europäische Klima führen. Die Arbeit beschreibt die Mechanismen, die mit dieser Inkonstanz einhergehen, und nennt mögliche Gründe dafür. Ein weiterer Teil konzentriert sich auf die Rolle von Anomalien der Meeresoberflächentemperatur, die bereits im Frühjahr sichtbar sind, und besonders in ihrer Variabilität mit dem tropischen Antrieb des Sommer-Ost-Atlantik-Musters in Verbindung zu stehen scheinen.

Contents

1 Introduction

As one of the Earth's densest populated areas, the prediction and understanding of climate processes and changes over Europe is of particular interest. Located in the mid-latitude westerlies, weather and climate in Europe are highly influenced by processes over the North Atlantic region. Patterns of geopotential height (GPH) in the middle troposphere have a big impact on the routes of low-pressure-systems that are the main drivers of the weather in Europe. Although most of the variability of these patterns is stochastic, they can also be driven by the tropics via tropical-subtropical teleconnections (*Trenberth et al.*, 1998). A better understanding of this tropical forcing could lead to more skillful seasonal predictions of European climate.

For boreal winter, many studies have been conducted on these teleconnections, mainly focussing on the winter North Atlantic Oscillation (NAO), the first mode of low-frequency variability over the North Atlantic (*Greatbatch*, 2000; *Hurrell et al.*, 2003). Despite being a free mode of variability, the NAO is partly influenced by diabatic heating anomalies in the tropics (*Yu and Lin*, 2016; *Scaife et al.*, 2017). *Scaife et al.* (2014) already showed the possibility of successful predictions of the winter NAO several months in advance due to this tropical forcing. Another study conducted by *Dunstone et al.* (2016) reported on skillful predictions more than a year ahead. Sources for this possible forecasting are predictable changes in the stratospheric polar vortex strength and climate variability in the tropical Pacific region. It was also shown that tropical forcing contributes for part of the trend in the winter NAO index between the 1960s and 2000s (*Greatbatch et al.*, 2003, 2012) and can be related to the anomalous cold winter of 1962/1963 (*Gollan and Greatbatch*, 2015).

Whereas in winter the strong westerly mean flow favors the propagation of Rossby waves, a main factor of the tropical-extratropical teleconnections, the jetstream shifts northward in boreal summer, reducing the mean flow and complicating the ongoing processes. Still, diabatic heating in the tropics can lead to upper-troposphere divergence which is an effective source of Rossby waves with possible influence on higher latitudes (*Sardeshmukh and Hoskins*, 1988). The most dominant mode of interannual variability in summer is the Summer North Atlantic Oscillation (SNAO) (*Hurrell and Deser*, 2010). Whilst this mode has strong influence on temperature and precipitation over Europe, *Folland et al.* (2009) showed that the SNAO is only weakly correlated to El Niño Southern Oscillation (ENSO) and therefore offers a limited and unclear amount of predictability. There is no evidence that the mode is connected to other tropical forcing. The SNAO comes with decadal to multidecadal variability that is mainly due to the influence of the Atlantic Multidecadal Oscillation (*Linderholm and Folland*, 2017).

Nevertheless, an interaction between the tropics and extratropics is also present in summer. *Ding et al.* (2011) performed maximum covariance analysis over the fields of boreal summer tropical rainfall and northern hemisphere (NH) geopotential height, detecting two patterns associated with the Asian summer monsoons. A circumglobal teleconnection (CGT) pattern in the mid-latitudes was found to be related to diabatic heating in the Indian summer monsoon (ISM) region in summers preceding an El Niño peak and a Western Pacific - North America teleconnection pattern was found to be connected to diabatic heating in the Western North Pacific summer monsoon (WNPSM) region in summers following El Niño. Another investigation focussing on the effects of diabatic heating in the monsoon areas was conducted by *Lin* (2009) and showed similar significant extratropical responses in the GPH-fields. *Lin* (2009) also presented evidence for an extratropical response in the southern hemisphere as a wave train over South America and the South Pacific was found to be connected to the WNPSM.

A study focussing on the tropical forcing of a regime over the North Atlantic European (NAE) region called the Summer East Atlantic (SEA) pattern was conducted by *Wulff et al.* (2017). This pattern is defined by the second Empirical Orthogonal Function (EOF) of 500hPa geopotential height of ERA-Interim reanalysis data over the period from 1979 to 2016 in the NAE region [90°W - 30°E; 40°N - 70°N]. Explaining 18.7% of interannual variance over this epoch, it is the second most important mode of low-frequency variability after the SNAO. The positive phase of the pattern is shown in Figure 1 and characterised by a dipole anomaly of geopotential height with a negative anomaly southwest of Iceland and a positive anomaly over central Europe. Similar patterns were identified by *Cassou et al.* (2005), called the Atlantic Low and causing warm temperature anomalies over France, and by *Iglesias et al.* (2014) who named it East Atlantic pattern and found a possible prediction by tropical sea surface temperature (SST).

The pattern is part of a circumglobal wave-train with certain similarities to those found by *Ding et al.* (2011) and *Lin* (2009), with high influence on European climate. It was shown that the pattern is strongly connected to high temperature anomalies over Europe, causing extremely hot summers in this area during positive SEA events. The SEA index, defined as the corresponding Principal Component (PC) time series for the EOF, is significantly correlated to the temperature records in Hamburg Fuhlsbüttel, explaining 26% of the variance which is even more than the 21% variance explained by the SNAO. Simultaneously, enhanced precipitation is found west of the British Isles and reduced precipitation over the Baltic Sea when the pattern is in its positive phase. It was shown that this connection can even remain present for certain extreme heat waves. *Wulff et al.* (2017) provided evidence that the European heat wave of 2015 took place when the SEA pattern was strongly positive in the 500 hPa-level. These strong impacts emphasize the need for better understanding of the driving mechanisms of the SEA pattern,

especially in times of an increasing number of those extraordinary hot events (*Coumou and Rahmstorf*, 2012).
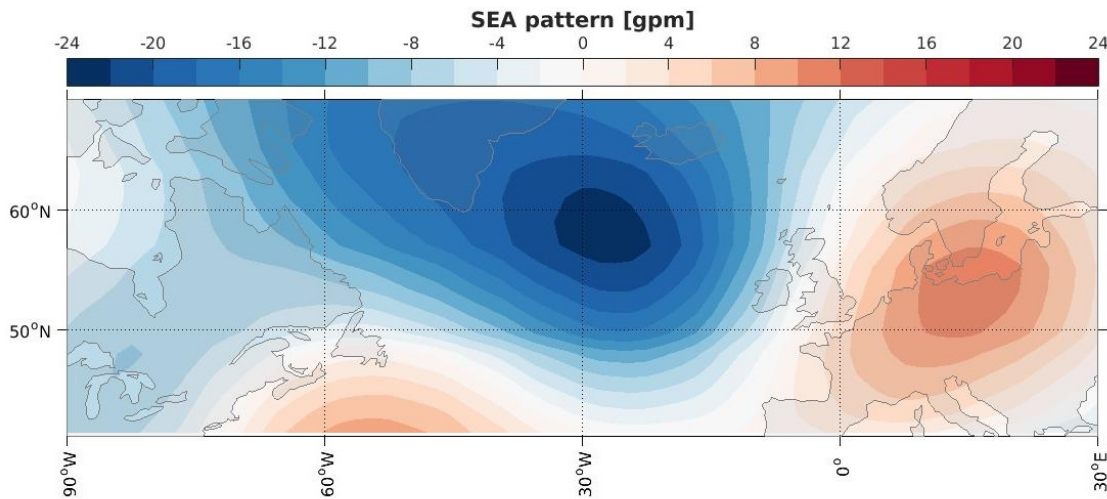

Figure 1: The SEA-pattern defined as the second EOF of summer (JJA) mean geopotential height anomalies at 500hPa over the North Atlantic European region [90°W - 30°E; 40°N - 70°N] in ERA-Interim reanalysis data over the period from 1979 to 2016. The pattern explains 18.7% of the interannual variance in summer season.

Apart from those local effects, it was found that the pattern is also correlated to precipitation anomalies in the tropical Pacific and Caribbean region. Figure 2 shows the regression of precipitation on the SEA index for ERA-Interim. Tropical convective precipitation anomalies cause diabatic heating anomalies that generate Rossby waves in this case propagating north-eastwards towards the North Atlantic and inducing the SEA pattern. As a measure of these precipitation anomalies, *Wulff et al.* (2017) introduced the Pacific Caribbean Dipole (PCD) index. This index is calculated by the difference of precipitation anomalies over a box in the tropical Pacific [180°W - 110°W; 10°N - 20°N] minus a box over the Caribbean [85°W - 65°W; 10°N - 25°N] in summer season (JJA). The boxes are illustrated in Figure 2. An exact definition can be found in section B in the appendix. The resulting index is correlated to the SEA index at 0.56 (significant at the 99% significance level).

One forcing mechanism of these dipole-like anomalies is the El Niño Southern Oscillation that has tremendous influence on tropical precipitation. It was shown that a developing El Niño is causing such a precipitation dipole in the tropics resulting in a strong correlation of the PCD index with the N34-index (defined as the area average of SST in the Niño 3.4-region in the tropical pacific as a measure of the intensity of ENSO. The index is defined precisely in section B in the appendix) of the following boreal winter (0.62 for JJA PCD-Index correlated with following March N34). Based on this and the

3

fact that the SEA index was also correlated with following March N34 at 0.47, *Wulff et al.* (2017) suggested that the SEA pattern may be a consequence of the developing El Niño, providing a certain amount of predictability of the pattern and its influence on European climate.
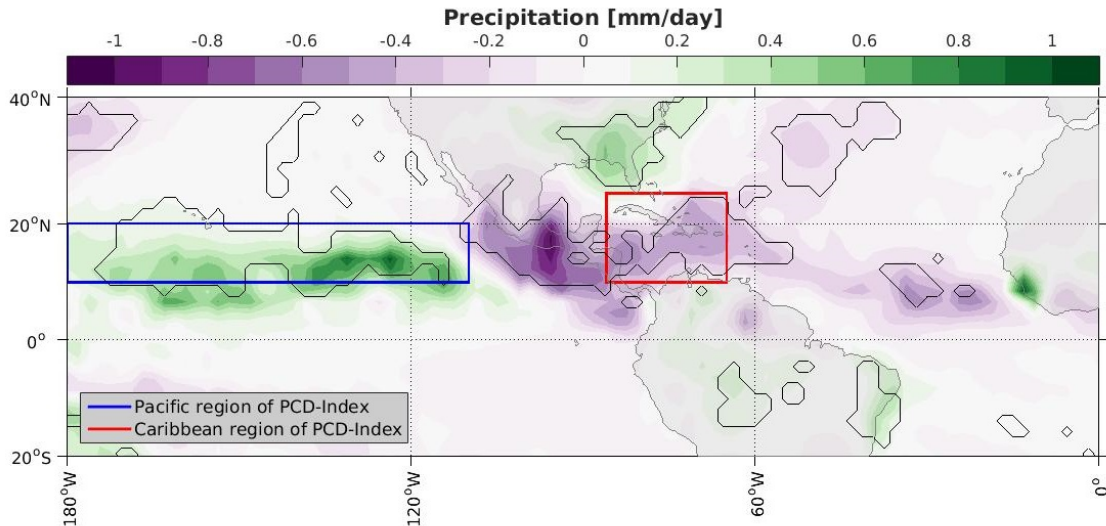

Figure 2: CMAP precipitation anomalies regressed on the SEA index of ERA-Interim reanalysis data. The black solid lines highlight the regions of statistical significance at the 95%-confidence-level according to a student's t test. The boxes show the averaging regions for the calculation of the Pacific Caribbean Dipole Index.

Ossó et al. (2018) found that a similar pattern that they called Summer East Atlantic pattern as well, defined by a positive anomaly in mean sea level pressure (MSLP) west of the British Isles, is strongly connected to SST anomalies in the North Atlantic in spring. They introduced a dipole SST-Index that shows significant correlations to their SEA index (defined as the July/August MSLP anomaly averaged over [25°W - 5°W; 45°N - 55°N]) already in early spring (March/April). They suggest that the pattern might therefore have seasonal predictability. *Wulff et al.* (2017) stated that a correlation to spring SST as it was already proposed before in *Duchez et al.* (2016) who suggested a connection between the 2015 heat wave and extreme cold SST anomalies prior to the event, does not contradict their results, however, *Wulff* (2018) does not think that the patterns defined in *Ossó et al.* (2018) and in *Wulff et al.* (2017) are the same thing.

Although the results of these studies are very reasonable, they were obtained using ERA-Interim reanalysis data which is only covering a period of nearly 40 years. It is known that internal climate variations often operate on time-scales much longer than these 40 years. However, due to the lack of availability of reliable observational data, it is necessary to take model runs into consideration to find out about longer-term variability.

For the winter season, an investigation on the connection between mega-ENSO (an important mode of the variation of global SST on interannual to interdecadal timescales (*Wang et al.*, 2013)) and the NAO was conducted by *Wu and Zhang* (2015). It was shown that the strong correlation that was present between 1957 and 1981 and was a good indicator for the winter NAO's tropical forcing, broke down in 1982 leaving almost no correlation thereafter. *Lee and Ha* (2015) provided evidence for significant changes in the tropical-extratropical teleconnection connected to the Asian summer monsoons. As stated before, the CGT pattern in the NH (introduced by *Ding et al.* (2011)) is correlated to the ISM and to the developing phase of ENSO. *Lee and Ha* (2015) found that the correlation to the ISM was stronger before the 1970s, but after that the CGT pattern was found to be more correlated to the developing phase of ENSO. A similar teleconnection change was found for the Western Pacific - North America pattern that is nowadays stronger influenced by the WNPSM and less by the decaying phase of ENSO. It was also shown that these changes in tropical forcing can contribute to a change in explained variance of the extratropical response, as the CGT pattern that is connected to the ISM and ENSO explains an enhanced 14.8% of the interannual variance of NH GPH after the shift instead of 9.8% before. Similar nonstationarities were found by *O'Reilly et al.* (2017) for the predictability of the Pacific North America pattern and the NAO in winter due to their tropical SST forcing. It was pointed out that over the period from 1900 to 2010 the forecasting skill varies extremely for both patterns, showing reasonable prediction skill for the period until 1940 and for the years from 1980 onwards but very poor skill in the middle of the 20th century. They conclude that the seasonal forecasting systems might be less useful in those periods of rather weak tropical Pacific SST forcing. It is possible that similar interdecadal variations are influencing the tropical forcing of the SEA pattern.

The aim of this study is therefore to investigate the SEA pattern and its tropical forcing in a model run with a length of 700 years and to address the questions, whether the findings of the study conducted by *Wulff et al.* (2017) can be verified in the model and whether they are constant over time or just represent a current state of the Earth system. For this purpose, a preindustrial control run of the Max-Planck-Institut Earth System Model was investigated that does not feature increasing greenhouse gases. Instead, the external forcing is constantly on preindustrial level providing valuable data to focus on internal variability. Similar to the findings of *Lee and Ha* (2015), it is possible that the tropical forcing of the SEA pattern is varying on larger time scales and understanding these variations would be of great significance for the climate in Europe now and in future developments. The relation between the tropical forcing of the pattern and the forcing by spring-SSTs in the North-Atlantic mentioned by *Ossó et al.* (2018) will be further investigated on these longer time scales as well.

The remainder of the study is structured as follows. First, there will be an overview of the used model configuration and datasets, as well as the methods used to obtain the results. Second, the results of the study will be presented, and last, the results will be summarized and discussed, especially in comparison to the current state of art of this topic.

2 Data and Methods

The following part will describe the datasets and methods used in this study. The first part will give a short overview of the datasets, their generation and their availability. The second part will explain the methods used in the analysis part of this thesis.

2.1 Data

This study is based on model output from a preindustrial control run of the Max-Planck-Institute Earth System Model (MPI-ESM) over a period of 700 years. ERA-Interim reanalysis data and CMAP precipitation data was used for comparison.

2.1.1 Model

The model description follows the explanation in the MPI-ESM overview paper from *Giorgetta et al.* (2013). The MPI-ESM is a fully coupled climate model that is part of the Coupled Model Intercomparison Project phase 5 (CMIP5) (*Taylor et al.*, 2012). It consists of general circulation models (GCMs) for the atmosphere (ECHAM6 *Stevens et al.*, 2013) and the ocean (MPIOM *Jungclaus et al.*, 2013) and subsystem models for land and vegetation (JSBACH *Reick et al.*, 2013) and marine biogeochemistry (HAMOCC5 *Ilyina et al.*, 2013). The MPI-ESM is the subsequent version of the ECHAM5/MPIOM coupled model that was used in CMIP3. OASIS3 is used as the coupler between the model's ocean and atmosphere components. This coupling is dependent on the surface fluxes of water, energy, momentum and CO2.

The output used in this analysis is produced by the model's atmospheric component, the atmospheric general circulation model (AGCM) ECHAM6, the newest version of the ECHAM series of atmospheric GCMs. The model consists of an adiabatic dynamical core based on the vorticity, divergence and thermodynamic equations, a model for the transport of scalar quantities and several physical parameterisations representing diabatic processes. Boundary data sets for external parameters such as trace gases, aerosols and solar irradiance are used as forcing conditions. Compared to its predecessor model ECHAM5, the newer version contains improvements concerning the radiation scheme, the computation of surface albedo and the convective triggering. The vertical resolution is also enhanced in the upper atmosphere with the highest pressure level moved to 0.01hPa (compared to 10hPa before), which allows an improved representation of the middle atmosphere's influence on high-latitude tropospheric circulation. The tropospheric vertical resolution, however, remains unchanged. A more detailed description on

7

the setup of ECHAM6 can be found in *Stevens et al.* (2013).

For the CMIP5 different configurations of the MPI-ESM were used. Most experiments were conducted with the low resolution version (MPI-ESM LR) that was also used in this thesis. This model configuration is based on a T63/1.9° (T63 is a triangular truncation at wave number 63) horizontal resolution on 47 hybrid sigma-pressure levels in the atmosphere and a bipolar (poles are moved to Greenland and the Weddell Sea coast) grid of 1.5° resolution at 40 z-levels in the ocean component.

The data used in this study was obtained by a preindustrial control (piControl) run over a period of 700 years. The experiment was conducted using constant forcing over time, based on constant orbital parameters (state of 1850), constant spectral solar irradiance (averaged over the solar cycle from 1844-1856), fixed greenhouse gas concentrations on preindustrial level (values of 1850) and monthly ozone concentrations computed as averages over the 11 years (length of a solar cycle) from 1850-1860. Aerosol forcing is limited to natural aerosols only and volcanic aerosol forcing is not present. Due to this constant forcing, this model experiment is explicitly suitable for investigations concerning long-term internal variability of the Earth system as it is the aim of this thesis.

This analysis made use of the output of several parameters of the atmospheric model component. Monthly means over a period of 700 years (that are labeled as the years 1-700, but do not correspond to our calender as the external forcing is on a level of around 1850) were computed from the output and regridded to regular latitude-longitude grids by using the spherical coordinate remapping and interpolation package (SCRIP). Parameters used in this study contain geopotential height at different pressure levels, mean sea level pressure, sea surface temperature (at the atmospheric horizontal resolution), surface air temperature, convective and large-scale precipitation, zonal and meridional wind at the 200hPa-level and velocity potential at the 200hPa-level.

2.1.2 Reanalysis data

As a comparison for the model data, ERA-Interim reanalysis data was used mainly to reproduce the findings of *Wulff et al.* (2017), for the period between 1979 and 2017. ERA-Interim is the global atmospheric reanalysis product of the European Centre for Medium-Range Weather Forecasts (ECMWF). The data is produced by a combination of available observations and prior information from a forecast model. By including the forecast model, it is possible to extrapolate information to unobserved parameters, areas and time steps in a physically meaningful way. Adjustments to observational information are then used to maintain consistency, resulting in high accuracy of the product. For more details on the production of the data see the official description of the configuration

and performance of the data assimilation system from *Dee et al.* (2011).

In this study, monthly outputs of several atmospheric parameters, including geopotential height, surface air temperature and sea surface temperature, were used and regridded to a regular latitude-longitude grid of 1.875° horizontal resolution to allow comparison to the model output. The data can be downloaded from the European Centre for Medium-Range Weather Forecasts.

2.1.3 Precipitation data

Precipitation data for the years from 1979-2017 is provided by the CPC Merged Analysis of Precipitation (CMAP) dataset. It is constructed from a combination of gauge observations and satellite-derived estimations. The data used in this study contains monthly means regridded to the same grid as before and can be downloaded from the National Oceanic and Atmospheric Administration.

2.2 Methods

In the following section, there will be a description of all the methods used in the analysis part of the thesis. Since this study focusses on interannual and longer-term variability, seasonal and more-monthly means were calculated from the monthly model data. Anomaly data were computed by removing the linear trend and time mean from each grid point. Different regimes were represented by indices where definitions can be found in section B in the appendix. Regression maps were calculated to relate these indices to other parameters.

To address the grid-box-size which is only constant in terms of latitude and longitude, but not concerning their covered area, special weighting techniques were used to calculate area averages and pattern correlations (section 2.2.1). To determine the dominant modes of interannual variability, Principal Component analysis was used in this study and will be explained in detail in section 2.2.2. Rossby wave guide and Rossby wave source analysis were conducted to investigate the propagation and source of Rossby waves in the model (section 2.2.4 & 2.2.5). All results were tested for statistical significance by using either the student's t test or the Monte-Carlo resampling technique. Both methods will be explained in section 2.2.6.

2.2.1 Area average and pattern correlation

As the original output data was regridded to a rectangular latitude-longitude grid, the resulting grid boxes become smaller towards the pole and bigger towards the equator. To take this into consideration, the calculation of area averages and pattern correlations was conducted by a weighting of the grid boxes with the cosine of latitude. The area average $\overline{x}$ of the M values x_i within the area is then calculated as

$$\overline{x} = \frac{\sum_{i=1}^{M} x_i \cos(lat(x_i))}{\sum_{i=1}^{M} \cos(lat(x_i))} \tag{1}$$

The pattern correlation r of two patterns $\boldsymbol{X}_1$ and $\boldsymbol{X}_2$ is calculated as the correlation coefficient of the grid points weighted by their represented box size

$$r = \frac{cov(\boldsymbol{X}_1, \boldsymbol{X}_2)}{\sqrt{var(\boldsymbol{X}_1)var(\boldsymbol{X}_2)}} \tag{2}$$

with

$$cov(\boldsymbol{X}_1, \boldsymbol{X}_2) = \frac{\sum_{i=1}^{M} \cos(lat(x_{1,i}))(x_{1,i} - \overline{x_1})(x_{2,i} - \overline{x_2})}{\sum_{i=1}^{M} cos(lat(x_{1,i}))} \tag{3}$$

the weighted covariance of both fields and

$$var(X_j) = \frac{\sum_{i=1}^{M} \cos(lat(x_{j,i}))(x_{j,i} - \overline{x_j})^2}{\sum_{i=1}^{M} \cos(lat(x_{j,i}))} \tag{4}$$

the weighted variance of field $\boldsymbol{X}_j$. The area averages $\overline{x_j}$ are calculated with the weighted area average technique introduced in equation 1.

2.2.2 Principal Component analysis

To obtain the most important modes of interannual variability, Principal Component analysis (PCA) was conducted on the fields of geopotential height at the 500hPa-level over the North Atlantic and sea surface temperature in the tropical Pacific. As climatological data often consists of recurring patterns, a high amount of variance can be explained by a little number of modes. The PCA aims to find that set of basis vectors (=the modes) that explains the highest amount of variance with the least number of these vectors. As they are orthogonal to each other, the resulting vectors are called the Empirical Orthogonal Functions (EOFs). In this case, the analysis was used to find the spatial patterns that explain the most variance over time. Hence, the data was transformed into a two-dimensional matrix $\boldsymbol{X}$ of the size $m \times n$ and the dimensions space

and time.

The problem of maximizing the amount of variance leads to the eigenvalue problem

$$(\boldsymbol{C} - \lambda \boldsymbol{I})\boldsymbol{e} = 0 \tag{5}$$

with $\boldsymbol{C} = \boldsymbol{X}\boldsymbol{X}^T N^{-1}$ the covariance matrix of $\boldsymbol{X}$ of size $m \times m$, λ the eigenvalue, $\boldsymbol{I}$ the identity matrix of size mxm, $\boldsymbol{e}$ the eigenvector and N the sample size. Solving this problem leads to a set of m eigenvectors (the EOFs) and corresponding eigenvalues that are all real and positive because $\boldsymbol{C}$ is symmetric. Ordering these EOFs according to their eigenvalues shows the most dominant modes of variability as the first EOFs. The ratio of the eigenvalue to the sum of all eigenvalues equals the amount of explained variance by the EOF:

$$var(\boldsymbol{e}_i) = \frac{\lambda_i}{\sum_{k=1}^{M} \lambda_k} \tag{6}$$

The transformation between the original data and the EOF space is done with the Principal Component matrix $\boldsymbol{Z} = \boldsymbol{E}^T \boldsymbol{X}$ with $\boldsymbol{E}$ containing the m eigenvectors as columns. $\boldsymbol{Z}$ contains information on the amplitude of every EOF at each time step resulting in m timeseries corresponding to the m EOFs, respectively, which are called the Principal Component (PC) time series. The data at every point of time can then be explained as the linear combination of the EOFs, multiplied with the corresponding value of the PC time series

$$\boldsymbol{X}_{i,n} = \sum_{j=1}^{M} \boldsymbol{E}_{i,j} \boldsymbol{Z}_{j,n} \tag{7}$$

To obtain information on the amplitude of the EOFs in units of the original dataset, the original data needs to be projected on the corresponding PC time series. This results in a regression map which is further explained in section 2.2.3.

To obtain the variance explained by an EOF for a limited period of time p that is different from the period used for the calculation of the EOF, one can construct a dataset $\boldsymbol{X}_{j,p} = \boldsymbol{E}_j \boldsymbol{Z}_{j,p}$ by using only the j-thEOF and its corresponding PC time series and compare the variance of this dataset to the variance of the original data in this period. The amount of explained variance by the EOF at each grid point i over the period of time p is given as

$$var(\boldsymbol{e}_{j,i,p}) = \frac{var(\boldsymbol{X}_{i,j,p})}{var(\boldsymbol{X}_{i,p})} \tag{8}$$

Applying the area average technique in equation 1 leads to the ratio of explained variance

for the desired field and time interval.

It is important to note that PCA is a mathematical deconstruction of the data set and therefore always finds dominant modes of variability although they do not necessarily need to represent a physical regime and have to be treated with care as was pointed out by *Dommenget and Latif* (2002). In most climatological applications, only the first few EOFs refer to real modes.

As the size of a sample is limited, there can be the problem of subsampling of the EOFs that was descriped by *North et al.* (1982). To estimate the sampling error they developed the North's rule of thumb that recommends only to use those EOFs whose eigenvalues are clearly distinct from the neighbouring ones by at least half its eigenvalue. Those cautionary notes were kept in mind during this study. For a more detailed description on the use of PC analysis in climatological data see the book from *von Storch and Zwiers* (1999).

2.2.3 Regression

For many climatological applications, it is important to relate known regimes to other regions or other parameters to find covariances and connections between these regions or parameters. In this study, use of regression maps is made to examine these connections. For every grid point k, a linear regression is calculated between the time series Y_k of the desired regressing parameter and the index time series i_X following the linear equation

$$Y_k = ai_X + b + \epsilon \tag{9}$$

The regression aims to find the best linear fit of Y_k to i_X by minimizing the error ϵ. The resulting value of a is in units of $\frac{[Y_k]}{[i_X]}$, but if the index time series i_X is normalized, the units of a will equal the units of Y_k. By repeating this analysis for all grid points, a map of regression coefficients is obtained that relates the parameter Y to a change of one standard deviation of the index time series i_X, which is one for normalized indices. The easiest way to calculate these coefficients is by matrix multiplication:

$$\boldsymbol{A} = \boldsymbol{Y} i_X N^{-1} \tag{10}$$

with N the sample size. Concerning the EOF, if $\boldsymbol{Y}$ is the original dataset used for the calculation of the EOFs and i_X is the PC time series, the resulting pattern $\boldsymbol{A}$ corresponds to the EOF with amplitude information in the original units of $\boldsymbol{Y}$. All the regression patterns in this study were tested for significance with a student's t test (section 2.2.6).

2.2.4 Rossby wave source analysis

Rossby waves are an important driver of the tropical-extratropical teleconnection and will therefore be analysed in this study. Rossby wave source (RWS) analysis is conducted to investigate the generation of Rossby waves by advection of vorticity by the divergent flow and vortex stretching in the upper troposphere (*Sardeshmukh and Hoskins*, 1988).

The nonlinear vorticity equation for the upper troposphere is

$$(\frac{d}{dt} + \vec{v} \cdot \nabla)\zeta = -\zeta\nabla \cdot \vec{v} + F \tag{11}$$

with $\vec{v}$ the horizontal flow field, ζ the absolute vorticity and F a frictional term. According to the Helmholtz decomposition every vector field can be split into the sum of a divergence-free and a rotation-free field. Doing that for the horizontal flow field leads to the sum of the rotation of a scalar field (the streamfunction) and the divergence of another scalar field (the velocity potential):

$$\vec{v} = \vec{v_\chi} + \vec{v_\psi} = \nabla\chi + \nabla_H \times \psi \tag{12}$$

with χ the velocity potential and ψ the streamfunction. Then the vorticity equation in 11 can be rewritten as

$$(\frac{d}{dt} + \vec{v_\psi} \cdot \nabla)\zeta = -\nabla \cdot (\vec{v_\chi}\zeta) + F \tag{13}$$

In this equation, the Rossby wave source is defined as

$$S = -\nabla \cdot (\vec{v_\chi}\zeta) = -\vec{v_\chi} \cdot \nabla\zeta - \zeta\nabla \cdot \vec{v_\chi} \tag{14}$$

The Rossby wave source consists of two terms which correspond to the advection of vorticity by the divergent flow ($\vec{v_\chi} \cdot \nabla\zeta$) and vortex stretching ($\zeta\nabla \cdot \vec{v_\chi}$).

Velocity potential is already an output variable from the model and the divergent flow component can be computed as the gradient of the velocity potential. The absolute vorticity was computed as the sum of planetary vorticity and relative vorticity

$$\zeta = f + \nabla_H \times \vec{v} \tag{15}$$

with f the Coriolis parameter. In this study, the analysis was conducted in the 200hPa level which is common practice for RWS analysis. A more detailed description on Rossby wave source analysis and an overview of climatological RWS can be found in *Shimizu and de Albuquerque Cavalcanti* (2011).

13

2.2.5 Rossby wave guide analysis

Apart from the formation of the Rossby waves, their propagation plays an important role for the tropical-extratropical teleconnection. Based on the fact that Rossby waves are refracted towards higher wavenumbers, their propagation usually follows waveguides which are local maxima of stationary wavenumber (*Hoskins and Ambrizzi*, 1993). The wavenumber of stationary Rossby waves K_S can be calculated from the horizontal mean flow and the meridional vorticity gradient via

$$K_S = \sqrt{\frac{\beta*}{\overline{u}}} \tag{16}$$

with $\overline{u}$ the zonal mean flow and

$$\beta* = \beta - \overline{u}_{yy} \tag{17}$$

the meridional gradient of absolute vorticity, with β the meridional gradient of planetary vorticity f and $\overline{u}_{yy}$ the meridional gradient of relative vorticity. The contribution of the meridional wind component to the relative vorticity has been neglected as in many other studies before (*Dawson et al.*, 2011). After the calculation the resulting wavenumbers are multiplied with the length of the corresponding latitude circle, resulting in the wavenumber per latitude, often referred to as *zonal* wavenumber in the literature. As the wavenumber is defined as a square root, two necessary conditions can be drawn for the propagation of Rossby waves which are a westerly mean flow and a positive meridional vorticity gradient. Areas of easterly mean flow or reversed meridional absolute vorticity gradient will strongly repel Rossby waves. Equation 16 shows that if easterly mean flow and reversed vorticity gradient work together, a calculation of the Rossby wavenumber is possible, however, there will be no propagation of Rossby waves. These regions where the waves will not propagate, will be highlighted in the plots. In this study, the zonal Rossby wavenumber was calculated based on the flow at the 200hPa-level. A more detailed explanation on the theory of Rossby wave propagation and the calculation of the wavenumber can be found in *Hoskins and Ambrizzi* (1993).

2.2.6 Statistical significance

As climatological data is highly stochastic, it is always necessary to differentiate between physically relevant results and random noise. To address this question, significance tests were established in science. In this study, only those results which are significant at the 95%-confidence level were interpreted.

During the analysis, regression of anomaly data on different indices was conducted (section 2.2.3). The resulting patterns were tested for statistical significance at the 95%-level by using the student's t test. An obtained value z_i at the i-th gridpoint was considered significantly different from zero, if

$$z_i > \frac{\sigma_{x_i} t}{\sqrt{N - 2 + t^2}} \qquad (18)$$

was true. Here, σ_{x_i} is the standard deviation of the i-th gridpoint over time, N is the sample size and t the significance threshold of the desired level and to the corresponding sample size. The results in this analysis were tested for the 95%-significance level for different sample sizes. The resulting values of t can be found in section C in the appendix. The regions of statistical significance will be highlighted in the plots.

To determine the significance of the correlation of two time series x and y with length N, a Monte Carlo resampling technique was used. For this purpose, time series were created by choosing two sets p_1 and p_2 of N random years. Then, the correlation $\rho_i = \rho(X(p_1), Y(p_2))$ of the resulting time series was calculated 1000 times, resulting in a distribution of the random correlations ρ_i. The correlation ρ of the original time series was considered significant, if it exceeded the mean of the random correlations by two standard deviations in either direction:

$$\rho > \overline{\rho_i} + 2\sigma_{\rho_i} \qquad (19)$$

$$\rho < \overline{\rho_i} - 2\sigma_{\rho_i} \qquad (20)$$

An example of one of these distributions can be found in Figure A.12 in the appendix. Monte Carlo resampling was also used for testing for the significance of pattern correlations. The threshold of two standard deviations was used, because it coincides with the 95%-confidence interval for normal distributions.

3 Results

3.1 The Summer East Atlantic pattern in the model

To identify the SEA pattern in the model run, Principal Component analysis was performed on the 500hPa-level of GPH (GPH_{500}) over the NAE region. Unlike in *Wulff et al.* (2017) the region for the analysis was chosen to be [90°W - 40°E; 20°N - 80°N] to extend the region more to the south. *Wulff et al.* (2017) decided to exclude the subtropical region following the suggestion of *Greatbatch and Rong* (2006) who found problems in the representation of GPH_{500} over North Africa in the ERA-dataset in summer season. However, the model run used in this study is not supposed to be affected by similar problems and hence, the subtropical Atlantic and North Africa will be included in the PCA. It was shown that the results are not sensitive to the exact choice of region.
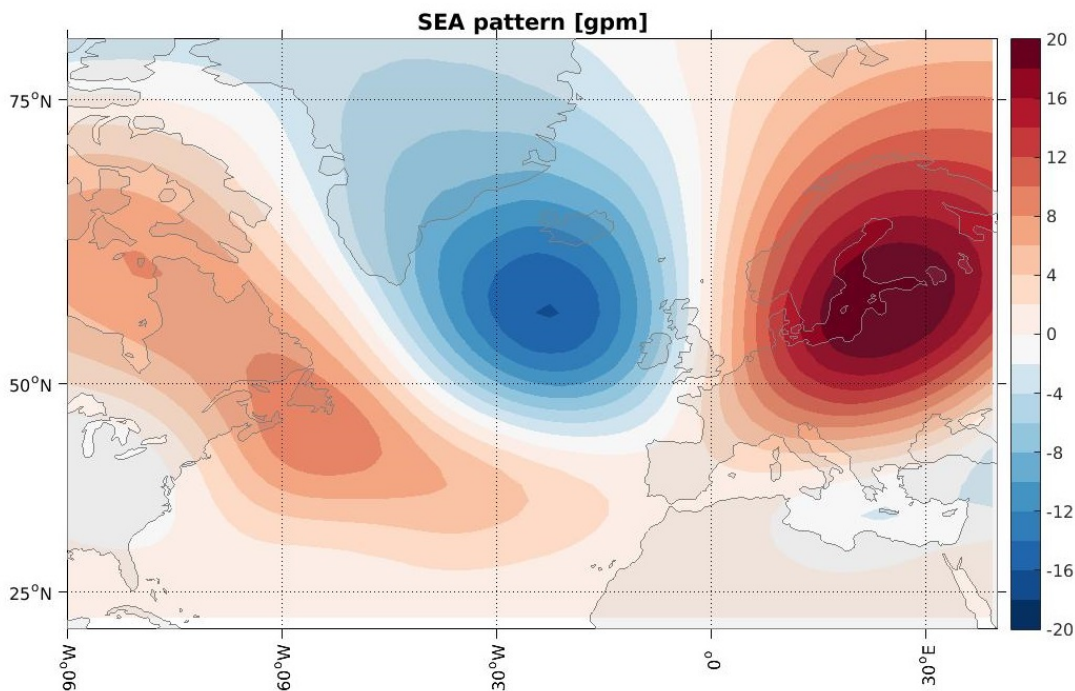
Figure 3: The SEA pattern in the model, defined as the third EOF of summer (JJA) mean geopotential height anomalies at 500hPa over the North Atlantic region [90°W - 40°E; 20°N - 80°N] over the whole 700 years of model output. The pattern explains 11.7% of the interannual variance in summer season.

Figure 3 shows the SEA pattern as it was found in the model as the third EOF of JJA GPH_{500} with an explained variance of 11.7%. The first two modes of which the first EOF corresponds to the SNAO can be found in Figure A.1 in the appendix. The eigenvalues of the first 3 EOFs are clearly distinct from the neighbouring eigenvalues according to

North's rule of thumb (*North et al.*, 1982). The SEA pattern is characterised by a strong dipole anomaly of GPH with a positive anomaly of 20 gpm over the Baltic Sea and the surrounding area and a negative anomaly of -20 gpm west of the British Isles and south of Iceland. Another positive anomaly with smaller amplitude (10 gpm) is found in the western North Atlantic. For further investigation, an index for the intensity of the pattern is introduced by the SEA index which is defined as the corresponding PC time series (a precise definition can be found in section B in the appendix).

Figure 4a) shows the regression of GPH_{500} on the SEA index. It can be seen that the pattern is part of a wave train in the mid-latitudes that extends further to the west with a negative anomaly over the eastern USA and the suggestion of a positive anomaly in the eastern North Pacific and to the east with a negative anomaly over western Asia, but is not circumglobal. The SEA pattern is robust at different pressure levels and remains present at mean sea level pressure (the regression of MSLP on the SEA index can be found in Figure A.3 in the appendix).
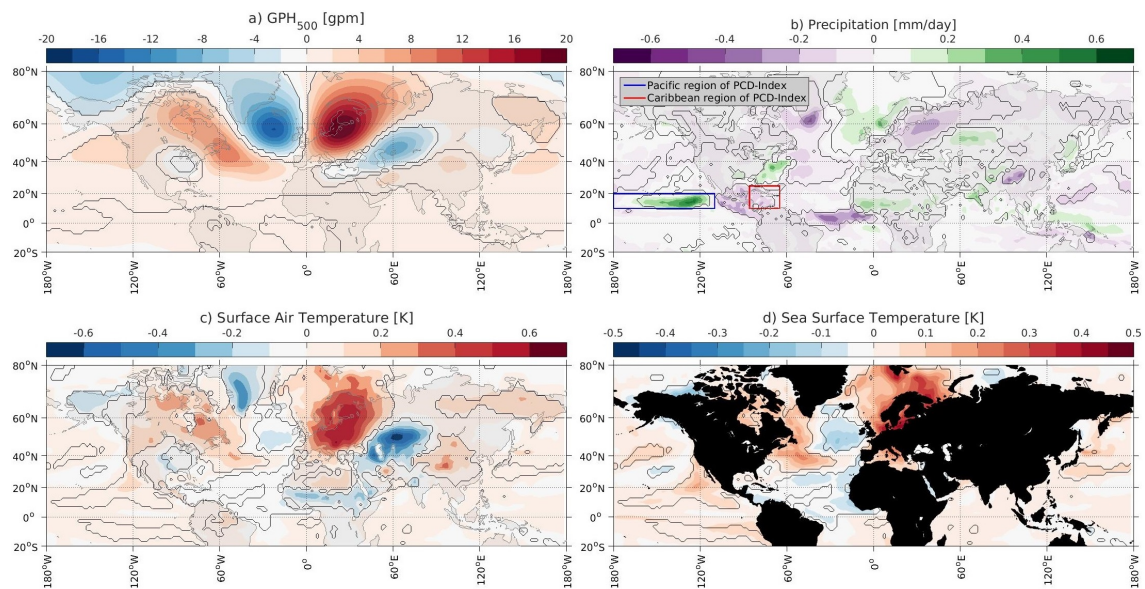

Figure 4: Regression of summer (JJA) a) geopotential height anomalies at the 500hPa-level, b) precipitation anomalies, c) surface air temperature anomalies and d) sea surface temperature anomalies on the SEA index as defined in section B in the appendix. The solid lines highlight the regions that are statistically significant at the 95%-level. The blue and red box in b) represent the regions for the calculation of the PCD index which is precisely defined in section B in the appendix.

Figure 4b)-d) shows the influence of the SEA pattern on European climate. The regression of the surface air temperature (SAT) on the SEA index (Figure 4c)) reveals a significant, positive temperature anomaly of more than 0.5K over most of Europe, especially in the Baltic Sea area and eastern Europe during positive SEA events. Simul-

taneously, SAT is reduced in western Asia, in the North Atlantic and in Greenland. These results are consistent with the regression of SST on the SEA index (Figure 4d)) which shows very high temperatures (up to +0.5K) in the Baltic Sea and North Sea when the SEA pattern is in its positive phase. Furthermore, a positive SEA event is related to higher temperatures in the Mediterranean Sea, the western North Atlantic and the Arctic Ocean, while the temperatures in the central North Atlantic are reduced. As seen in Figure 4b), the SEA pattern is also strongly related to precipitation over Europe. In its positive state, it is connected to enhanced precipitation over the British Isles, the North Atlantic and Scandinavia (+0.2 mm/day). Simultaneously, reduced precipitation is found over eastern Europe and northern Russia (-0.2 mm/day). The precipitation over central Europe shows no significant response.

3.2 Tropical forcing of the SEA pattern

Apart from the local impacts of the SEA pattern, the regressions (Figure 4) also reveal significant connections to the tropics. The positive phase of the SEA pattern is significantly related to strong positive anomalies of precipitation over the tropical Pacific and negative anomalies over the Caribbean and Central America, forming a dipole between these two regions. This response of tropical precipitation is mainly due to convective precipitation, whereas the local impact in Europe is large-scale precipitation (the regression of convective precipitation can be found in Figure A.3b) in the appendix) These features are also seen in the regressions of SAT and SST, showing a dipole between the eastern tropical Pacific and the southern Caribbean region, but their response is rather weak compared to the amplitude that is found in Europe. The precipitation dipole, however, is of even higher amplitude than the signal in Europe, reaching positive anomalies of up to 0.5 mm/day and negative anomalies of -0.4 mm/day, compared to 0.2 mm/day in Europe.

In order to further investigate this tropical-extratropical teleconnection, the Pacific Caribbean Dipole (PCD) index is used following the study of *Wulff et al.* (2017). The index is defined as the normalized difference of precipitation anomalies averaged over the Pacific region [180°W-110°W; 10°N - 20°N] minus the Caribbean region [85°W - 65°W; 10°N - 25°N], represented by the boxes in Figure 4b). Over the 700 years the PCD index is correlated to the SEA index by $\rho=0.17$ which is statistically significant at the 95%-confidence level according to Monte Carlo resampling.

Investigating the PCD's influence on Europe by regressing GPH_{500} on the index (Figure 5) reveals a clear wave train-like pattern over the North Atlantic with a negative anomaly south of Iceland and west of the British Isles and a positive anomaly over

eastern Europe. Although the pattern has high resemblance with the SEA pattern over Europe and the eastern North Atlantic, the anomaly centres are slightly shifted to the south compared to the SEA pattern defined as the EOF (Figure 3), and discrepancies appear in the northwestern and southwestern corner of the NAE box, resulting in a pattern correlation of 0.58 that is not significant at the 2σ-threshold according to Monte Carlo resampling.
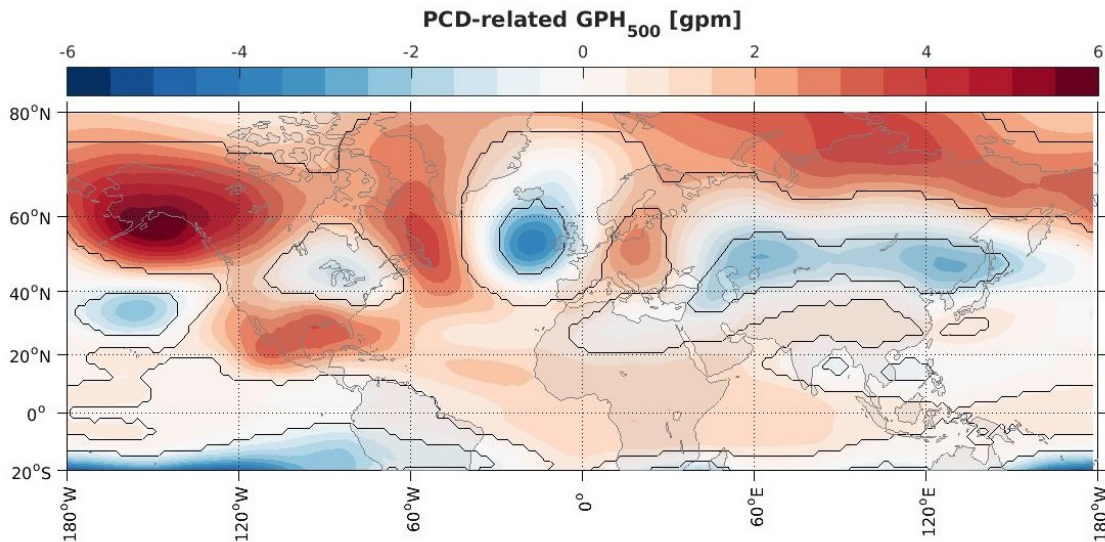

Figure 5: Regression of summer (JJA) anomalies of GPH_{500} on the PCD index as defined in section B in the appendix (see the boxes in Figure 4b)). The solid lines highlight the regions of statistical significance at the 95%-level.

3.3 Nonstationarity of the SEA pattern

The results mentioned above were obtained by investigating the whole model run that covers a length of 700 years which is more than 15 times as large as the ERA-Interim reanalysis dataset that was used in the study of *Wulff et al.* (2017). This section will therefore deal with the variability of the findings of section 3.1 & 3.2 within these 700 years. For this purpose, the model run was divided into small periods of 51 years which were then analysed in terms of variance explained by the SEA pattern and correlation to the PCD index. Figure 6 shows the running correlation between 51 years of SEA index and PCD index and the variance explained by the SEA pattern for the same periods. An interval of 51 years is represented by the year in its centre. It is visible that both the correlation and the explained variance are not constant over time, but highly variable on different timescales. The correlation between SEA and PCD remains rather low during most of the time, with correlation coefficients that indicate effectively no correlation at all (grey filling in Figure 6), but shows some peaks (green filling in Figure 6) with

signifcant correlations of more than 0.28 with the third peak lasting for almost a hundred years (years 300-400). In this episode, the correlation grows to its largest value of 0.58 (years 307-357). The resulting correlation coefficient of 0.17 for the whole 700 years is a good compromise between these periods of high correlation and those with lower correlation.
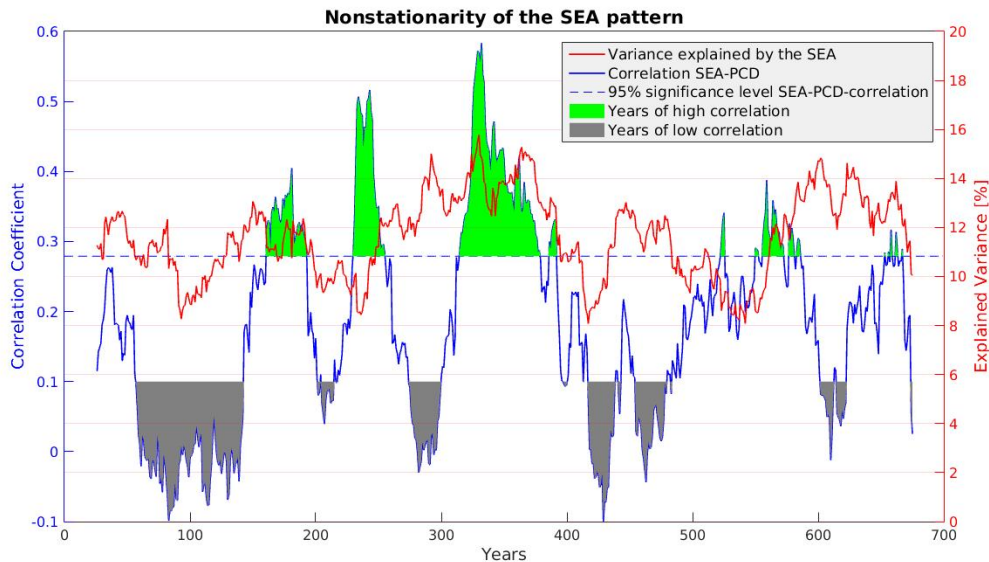

Figure 6: The blue line shows the running correlation of 51-year windows between the SEA index and the PCD index. The value of a certain year represents the 51 years surrounding this year (± 25 years). The blue dotted line shows the 2σ-significance threshold due to Monte Carlo resampling. Green filling indicates years of high correlation with coefficients higher than the 2σ-threshold, grey filling indicates low correlation (correlation coefficient lower than 0.1). The red line shows the variance explained by the SEA pattern for the 51-year interval around the respective year.

The variance of the SEA pattern shows some ups and downs as well, but the variations are in general lower, with a minimum value of 8.1% (years 392-442) and a maximum value of 15.8% (years 305-355), but still there are periods of lower explained variance and those with higher explained variance. For most of the time, there is no clear connection between both curves in Figure 6 visible, but there are certain periods where a relation seems present. Between year 57 and 142, the correlation between the SEA and the PCD is very low over quite a long time (grey filling for 86 consecutive years), and in this epoch, the variance explained by the SEA pattern reaches very low values of only 8-10%. The other extreme can be found in an episode of constantly very high PCD-SEA-correlation (years 315-378, green filling for 64 consecutive years) where both the absolute maximum of PCD-SEA-correlation (0.58) and of explained variance (15.8%) are located, and the variance does not drop below 12%. However, for most of the other years the connection between the PCD-SEA-correlation and the variance explained by the SEA pattern is less

clear. Still, both graphs seem to have a relation as the correlation coefficient for the whole period is 0.29 which is statistically significant at the 95%-level.

Regarding the frequency of these variations, there is a constant succession of high PCD-SEA-correlations and low correlations visible in the first half of the model run, but the duration of the events is variable. Between these epochs (between the grey and green filling) the correlation changes very fast. For the second half of the model run, there is no clear pattern in the succession of periods of low correlation and high correlation visible, and there are more time periods that are neither significant nor clearly non-significant (no filling).

Apart from the variations of the tropical forcing of the SEA pattern and its explained variance, it can also be shown that the pattern itself is not constant over time. By doing Principal Component analysis over smaller periods of only 51 years (not shown) and investigating the resulting patterns the SEA pattern's development over time was analysed. As the dominance of the SEA pattern was found to be varying, it was chosen to be represented by the one out of the first five EOFs that is most similar to the SEA pattern defined as the third EOF of the whole 700 years according to pattern correlation.

It was found that there are periods where the PCA reveals a pattern that is very similar to the 700-year-SEA-pattern (pattern correlation of >0.8) as the second or third dominant mode. However, also epochs were found where none of the first five EOF patterns represented the SEA pattern well (with a maximum pattern correlation of 0.5). Similar to the previous results, no constant relation can be drawn to the explained variance or the PCD-SEA-correlation. However, there are epochs of common features. It has to be stated here that the resulting eigenvalues of the EOF patterns are not always clearly distinct from one another according to North's rule of thumb (*North et al.*, 1982) and therefore have to be interpreted carefully. Still, this does not contradict the general result of the nonstationarity of the SEA pattern in the EOFs.

3.3.1   Periods of high PCD-SEA-correlation

In order to further investigate the nature of the nonstationarity the following section will focus on the periods of high correlation between the PCD index and the SEA index. For this purpose, those years in the middle of a 51-year window with a correlation significantly different from zero were selected and defined as *years of high PCD-SEA-correlation*. By applying this criterion 166 years were chosen which are marked by the green filling in Figure 6. The regression of the other parameters was then repeated for these years.

In general, the SEA pattern's impact on European climate remains very similar. As seen in Figure 7c) the positive SEA pattern is still related to positive temperature anoma-

lies over most of Europe that are statistically significant. The temperature response is very similar to Figure 4c), the positive anomaly over Europe is only slightly shifted north-westwards and the response over the Arctic Ocean and Greenland is intensified. In the precipitation regression, there is still a dipole visible over Europe, with enhanced precipitation over the British Isles, the North Atlantic and Arctic Ocean, and reduced precipitation over eastern Europe, but the response over Sweden and Finland is no longer significant. The amplitude of the anomalies in Britain and eastern Europe are slightly enhanced. The response of SST (Figure 7d)) is strengthened, now covering the Baltic Sea, the North Sea, the Labrador Sea and most of the North Atlantic and Arctic Ocean with a partly enhanced amplitude.
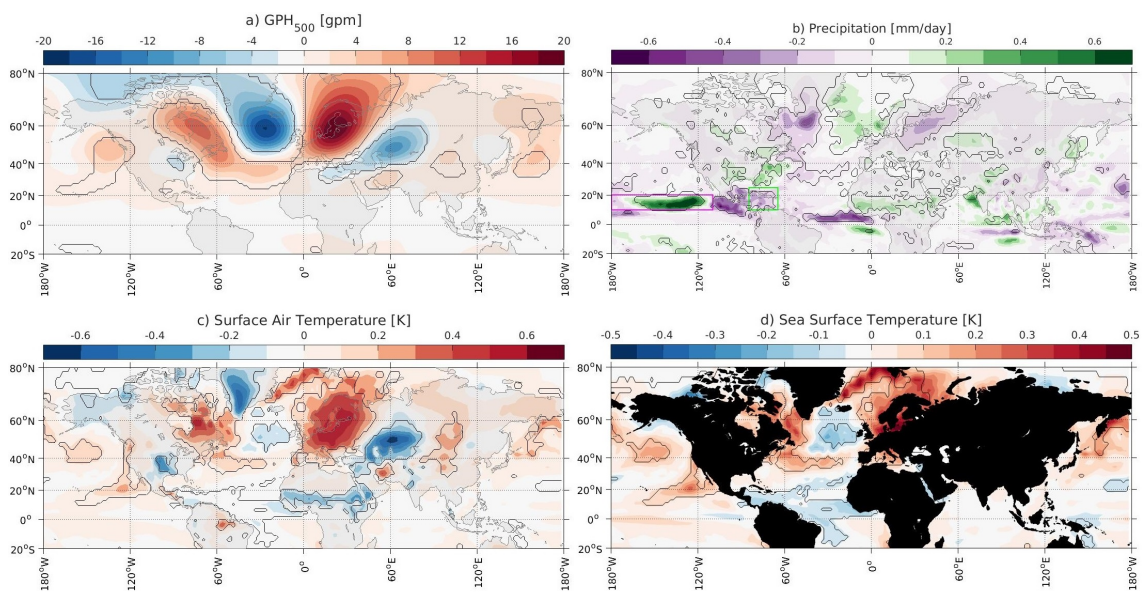
Figure 7: Same as in Figure 4, but only for the years of high correlation, marked by the green filling in Figure 6.

The relation to the tropics shows a strongly intensified response. A clear dipole appears in the fields of SAT and SST with higher temperatures in the eastern tropical Pacific and reduced temperatures in the Caribbean, both significant at the 95%-confidence level. The amplitude is slightly enhanced compared to the regression for all 700 years. A more intense amplification is visible in the regression of the precipitation, resulting in a very strong precipitation dipole over the tropical Pacific and Caribbean, with an amplitude of 0.7 mm/day over the Pacific and -0.3 mm/day over the Caribbean. The biggest part of the negative anomaly is now located over Central America and not covered by the calculation box of the PCD index. The amplitude of the dipole is outstanding compared to the other precipitation responses, even in Europe. The regression of the GPH_{500} on the PCD index (Figure 8) results in a clear wave train-like pattern in the northern hemisphere, including the SEA pattern over the North Atlantic. The amplitude of the

anomaly centres now reaches values of 6 gpm which is around 30% of the overall amplitude of the SEA pattern and more than in Figure 5. However, only the centres of the anomalies over the NAE sector are statistically significant. Over the North Atlantic and Europe, the regression is in good agreement to the SEA pattern resulting in an enhanced pattern correlation of 0.72 which is significant according to a Monte Carlo resampling test.
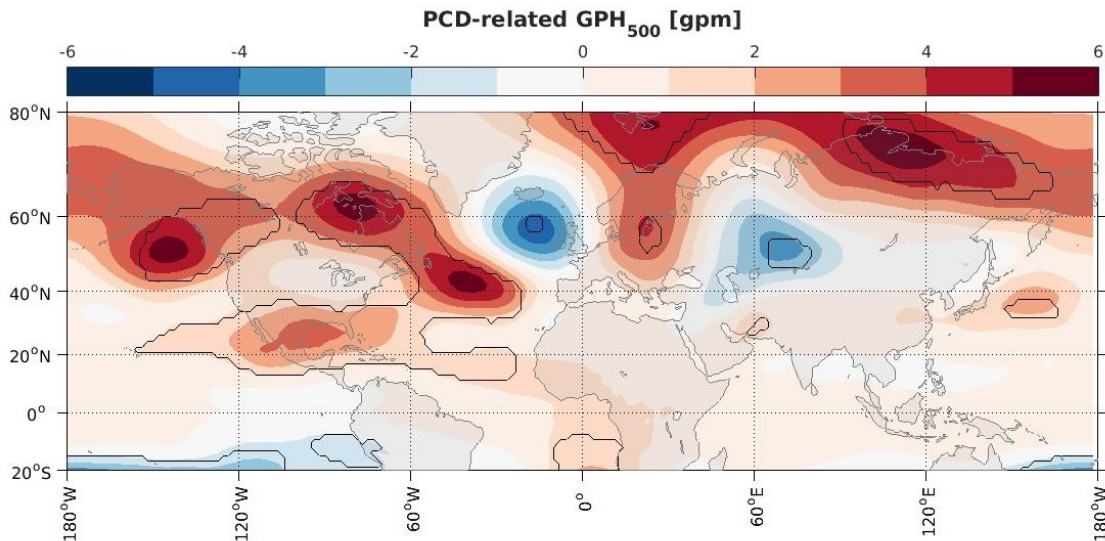

Figure 8: Same as in Figure 5, but only for the years of high correlation marked by the green filling in Figure 6.

3.3.2 Periods of low PCD-SEA-correlation

Similar to what was done in the previous section, periods of low correlation between the SEA index and the PCD index were selected from Figure 6. Those 51-year intervals with a PCD-SEA-correlation of less than 0.1 were chosen to be represented by the years in the middle of these intervals, resulting in a sample of 203 *years of low PCD-SEA-correlation* highlighted in grey in Figure 6. The resulting regression patterns for these years are pictured in Figure 9. The influence on European climate remains quite similar, as the regressions of SAT and SST still show positive temperature anomalies over central Europe, the Mediterranean and the North and Baltic Sea, and the precipitation response of the SEA pattern is still positive over the British Isles and negative over eastern Europe, when the pattern is in its positive state. Compared to the years of high correlation in Figure 7, the temperature anomalies are only slightly reduced in terms of amplitude and covering a smaller region. In comparison to the results in Figure 4, one can see responses of rather similar spatial extent and amplitude, but with some differences east of Greenland where no significant temperature signals can be found for the

years of low SEA-PCD-correlation. The regression of mean sea level pressure (shown in Figure A.4a), b) in the appendix) reveals reduced robustness of the SEA pattern in its vertical extent, as the amplitude of the MSLP response is reduced in the years of low correlation (Figure A.4b)) compared to the years of high correlation (Figure A.4a)). Despite these small differences the influence of the SEA pattern on European climate remains clearly significant and unchanged in its main features. Air temperatures and sea surface temperatures are enhanced over Europe, precipitation is enhanced over Ireland, Scotland and western Scandinavia and reduced over eastern Europe and western Russia, when the SEA pattern is in its positive state.
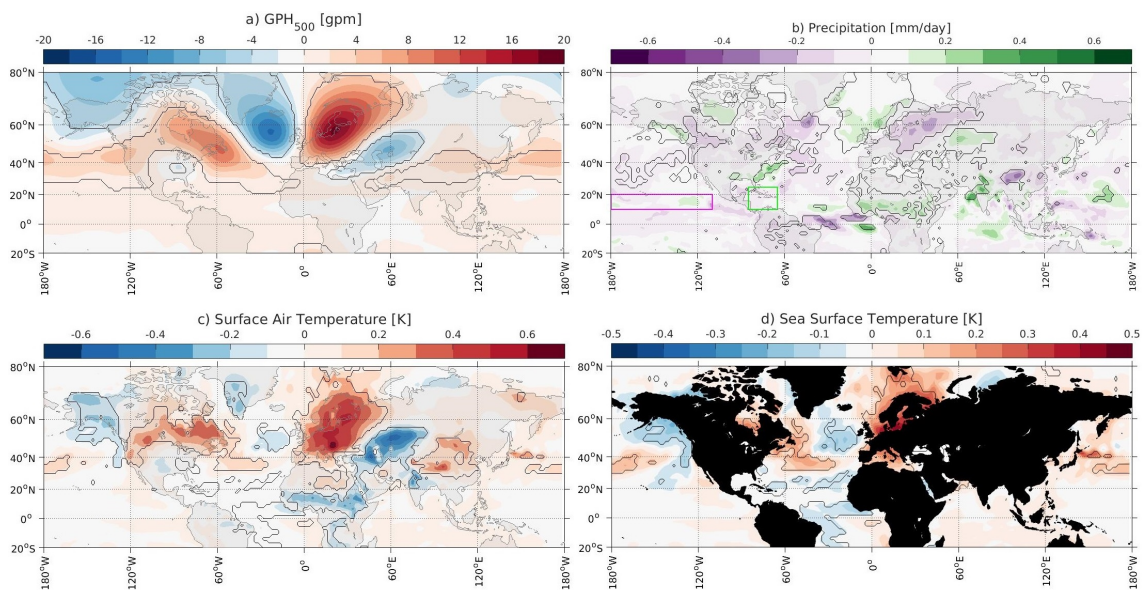

Figure 9: Same as in Figure 4, but only for the years of low correlation, marked by the grey filling in Figure 6.

A completely different result emerges for the tropical response. There are no significant temperature signals to be seen in either SST or SAT in the tropical Pacific and the Caribbean apart from a small, weak cold anomaly in the eastern Caribbean. The precipitation signal does not show a significant response in these areas either. The resulting pattern of precipitation consists of weak, non-significant anomalies with no resemblance to the PCD. It seems that the SEA index is not correlated to tropical activity in the Pacific and Caribbean during these years at all, which results in a pattern of GPH$_{500}$ regressed on the PCD index (Figure 10) that differs from the previous ones (Figure 5 & 8). Although the regression still shows wave train-like features in the NH and even a negative anomaly west of Britain and south of Iceland, similar to the one in the SEA pattern, this anomaly extends eastwards over Scandinavia towards eastern Europe. The other main characteristic of the SEA pattern, which is a positive GPH anomaly over the Baltic Sea is not visible. Hence, the regression pattern is clearly different from the SEA

pattern, resulting in a pattern correlation of 0.01. Instead, the regression is dominated by a strong positive GPH anomaly over Alaska and the northern Pacific and a weaker negative anomaly south of that.
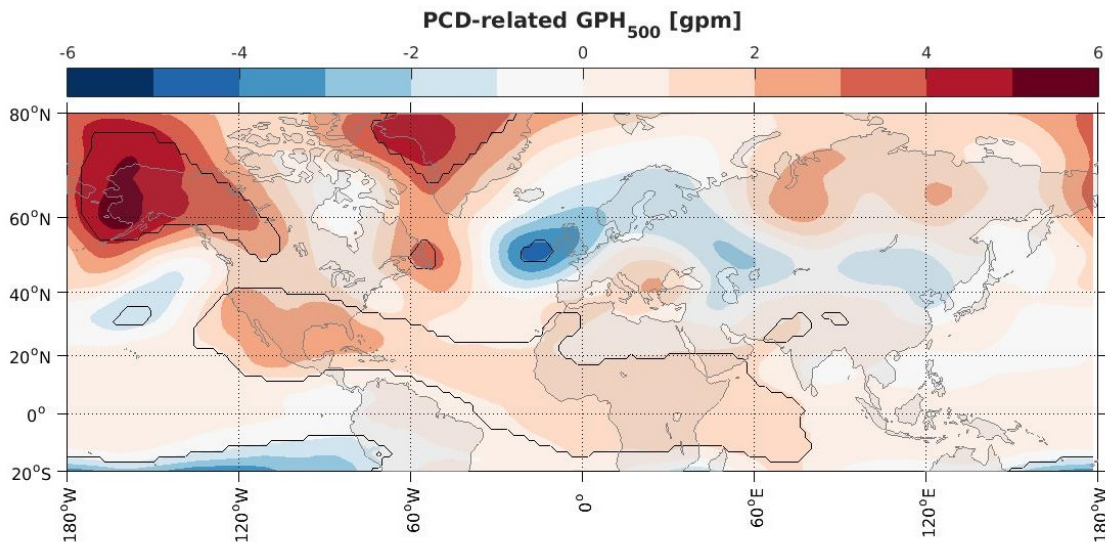

Figure 10: Same as in Figure 5, but only for the years of low correlation marked by the grey filling in Figure 6.

3.4   Drivers of the tropical forcing

As presented in the previous sections, the tropical forcing of the Summer East Atlantic pattern is highly variable. In order to find possible reasons for this nonstationarity, this section will focus on comparing the responsible mechanisms for two shorter time intervals that represent the extremes of the tropical-extratropical teleconnection. For this purpose, the longest continous intervals of very high PCD-SEA-correlation and effecitvely no correlation were selected from Figure 6. An interval of 71 years between 65-135 was chosen to represent a constant lack of tropical forcing (grey filling during this epoch in Figure 6) with a correlation between the PCD index and SEA index of -0.05. The SEA pattern only explains 10.4% of the interannual variance over the NAE region during the period.

An interval of 101 years between 300 and 400 was selected to represent constantly high PCD-SEA-correlation (green filling during this epoch in Figure 6). With a correlation of 0.39 the SEA index is highly related to the PCD. It is also a period of high variance explained by the SEA pattern (14.1%).

25

3.4.1 The influence of ENSO

It was suggested by *Wulff et al.* (2017) that the SEA pattern can be related to the developing ENSO, via the Pacific Caribbean precipitation dipole. This section examines whether ENSO contributes to the lack of robustness of the tropical forcing. To determine this influence, ENSO was defined as the first EOF of November-March (NDJFM) sea surface temperature over the tropical Pacific [120°E - 100°W; 30°S - 30°N] (Figure A.2 in the appendix) and the corresponding PC time series as an index for ENSO. The resulting pattern and the index are a good representation of ENSO as the index is correlated to the NDJFM Niño 3.4-index at 0.92. Regressing the precipitation anomalies of the previous boreal summer (JJA) on this index (Figure A.6 in the appendix) reveals a clear precipitation dipole over the tropical Pacific and the Caribbean that is very similar to the one associated with the SEA pattern (the PCD) for both epochs introduced above. This constant influence of ENSO on the PCD is supported by the correlation between the ENSO index and the PCD index which is 0.49 for 65-135, 0.44 for 300-400 and 0.45 for the whole 700 years. The running correlation (shown in black in Figure A.11 in the appendix) reveals some more variations for this correlation, but it hardly ever drops under the 95%-significance threshold, suggesting that the developing ENSO is constantly producing the PCD. The correlation between ENSO and the SEA index, however, is highly variable (red line in Figure A.11 in the appendix). For the epoch of very low tropical forcing (65-135) ENSO is not correlated to the SEA index (-0.03), but the relation is higher for the period of strong tropical forcing and SEA-influence (300-400) with a correlation coefficient of 0.21 which is statistically significant. The overall correlation for the whole 700 years is 0.09 and not significant. Although the value of 0.21 is significant at the 95%-level and a direct relation between ENSO and the SEA pattern is more present during this epoch as the regression of GPH_{500} (JJA) on the following winter (NDJFM) ENSO (Figure A.5 in the appendix) shows some features similar to the SEA pattern, the resulting pattern correlation of 0.61 is not significant at the 95%-level. The pattern correlations for the regressions of the years 65-135 (Figure A.5b)) and the whole 700 years are -0.25 and 0.04 and not significant.

3.4.2 Rossby wave propagation

As mentioned before (section 1), tropical-extratropical teleconnections are mainly driven by Rossby waves. To investigate these Rossby waves, the following section will analyse the propagation of Rossby waves in comparison for the two time intervals introduced in section 3.4. Figure 11 shows the zonal Rossby wavenumber for both periods of time. In this plot, local maxima can be interpreted as waveguides as the Rossby waves are refracted towards higher wavenumbers and therefore tend to follow those waveguides

(*Hoskins and Ambrizzi*, 1993). The solid black line highlights the wavenumber 5 that is typical for tropical-extratropical teleconnections. The waveguide that is responsible for the tropical forcing of the SEA pattern extends eastwards from the tropical Pacific at around 15°N over the southern United States towards the North Atlantic and Europe. However, this waveguide is clearly present in both periods, showing just little differences in western Europe, where it is connected to another waveguide running over southern Europe towards Asia in the years 300-400, but not in the years 65-135. Between the tropical Pacific and the North Atlantic, no relevant differences can be found. Similar results were found for the comparison of the mean circulation in the upper troposphere during both epochs (not shown).
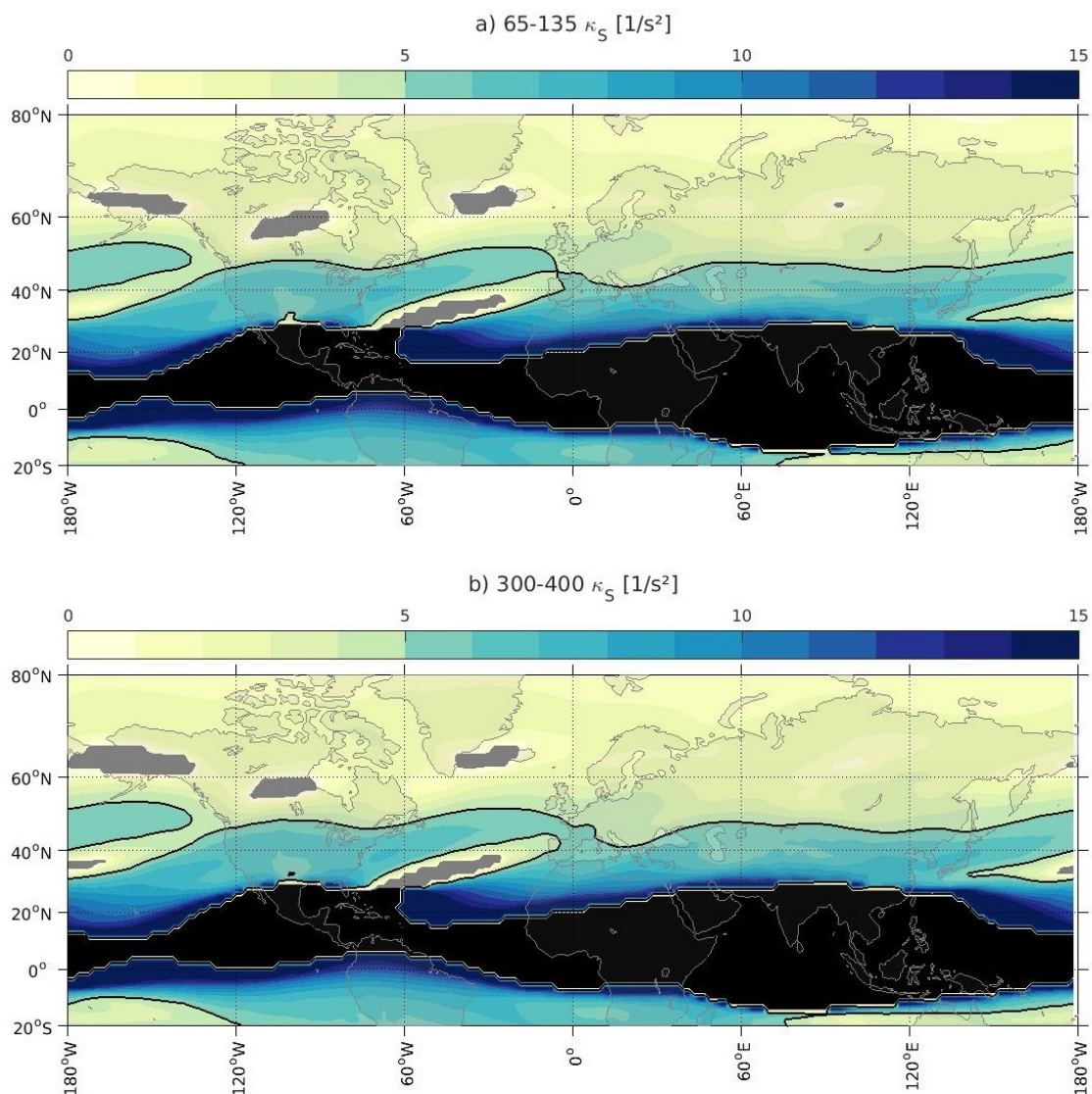

Figure 11: Stationary Rossby wavenumber per circle of latitude for the years a) 65-135 and b) 300-400. The solid black line indicates the wavenumber 5. Black filling represents areas with an easterly mean flow, grey filling indicates a reversed meridional vorticity gradient that strongly repels Rossby waves.

3.4.3 Rossby wave source

Another possible driver for the nonstationarity could be a different generation of Rossby waves. For this purpose, the PCD and SEA-related Rossby wave source is shown in Figure 12. The main region for the generation of Rossby waves driving the tropical-extratropical teleconnection of the SEA pattern is the Caribbean region. For both, the SEA-related and the PCD-related RWS, positive RWS is found throughout the Caribbean, while negative RWS that is not producing Rossby waves is present over the tropical Pacific. In comparison of the two different epochs, the SEA seems to be related to positive RWS in a small part of the Caribbean and the North Atlantic for the years 65-135. In the epoch from 300-400, however, a bigger part of the Caribbean and Central America is a region of generation of Rossby waves. In the mid-latitudes, there are also big differences between both epochs to be seen.

The Rossby wave source that is associated with the PCD index shows a rather consistent response. Negative Rossby wave source is found over the tropical Pacific where the Pacific part of the PCD is located. Positive RWS is found over the Caribbean PCD box, extending northeastwards over the Atlantic ocean. By comparing both periods of time, it becomes clear that the general signal of Rossby wave source associated with the PCD index is very similar. However, the response for the years from 300-400 (very strong tropical forcing) is enhanced compared to the years from 65-135 (low tropical forcing).
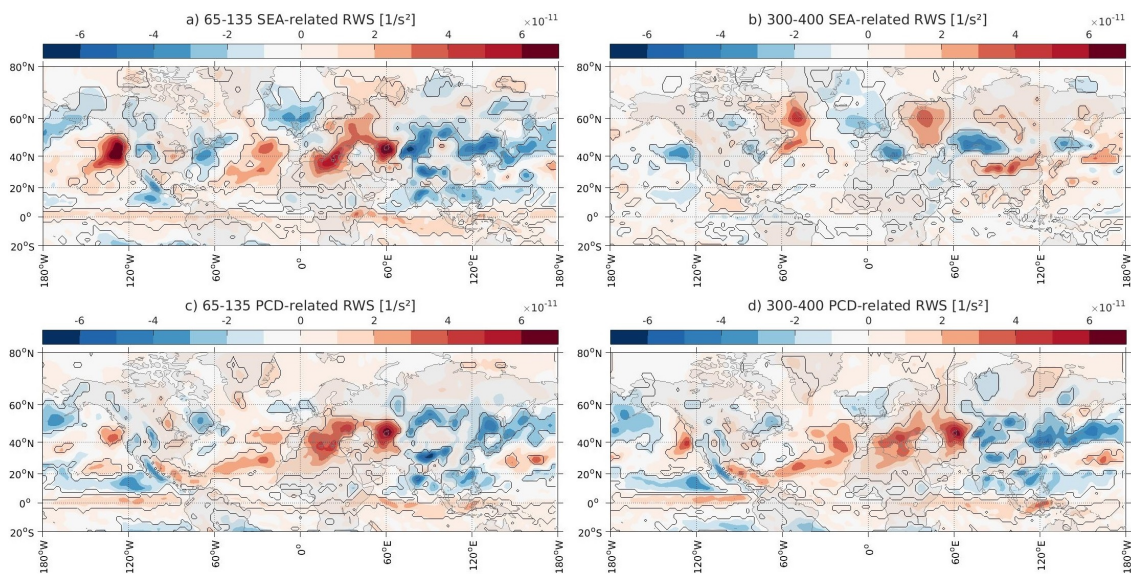

Figure 12: Summer (JJA) Rossby wave source regressed on the SEA index (a),b)) and the PCD index (c),d)) for the years from 65-135 (a),c)) and 300-400 (b),d)). The solid black lines indicate statistical significance at the 95%-level. The RWS was calculated with seasonal means for summer (JJA).

3.5 Influence of spring sea surface temperature

In former studies, an influence of spring SST on European summer climate patterns like the SEA pattern was suggested (*Wulff et al.*, 2017; *Ossó et al.*, 2018). In this section, the impact of spring (March/April (MA)) SST in the North Atlantic on the SEA is investigated. Although a regression of the MA-SST on the SEA index of the following summer (Figure A.10 in the appendix) does not produce relevant results for the whole 700 years of model output, there is a significant response visible in the North Atlantic for the period of 300-400. As shown in Figure 13b) the positive SEA phase is related to a strong cold anomaly in the gulf stream region and light warm anomalies in the rest of the North Atlantic. To further analyse the relation between this anomaly and the SEA index a dipole SST index introduced by *Ossó et al.* (2018) is used. It is calculated as the difference of spring (MA) SST-anomalies between a northwestern box [52°W - 42°W; 40°N - 48°N, green in Figure 13] and a southeastern box [35°W - 20°W; 35°N - 42°N, magenta in Figure 13] (exact definition in section B in the appendix). However, these boxes only cover part of the significant cold anomaly in the northwestern box, but there is no significant response visible in the other box. Figure 13a) shows the regression for the period 65-135: Here, the SST pattern looks entirely different, with slightly enhanced temperatures in the northern North Atlantic and reduced temperatures in the subtropical North Atlantic. The boxes do not agree with any outstanding significant anomalies.
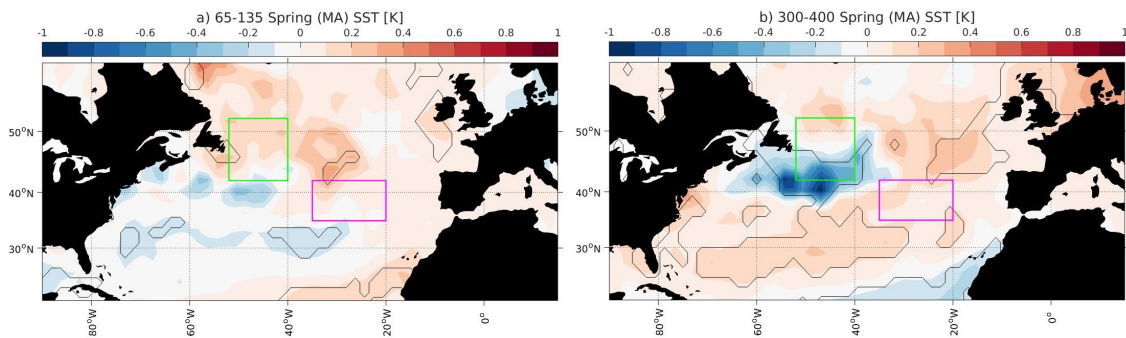

Figure 13: Spring (March,April) SST regressed on the following summer (JJA) SEA index for the years a) 65-135 and b) 300-400. The solid lines indicate 95%-significance. The green and magenta box highlight the averaging regions for the calculation of the Spring SST dipole index introduced by *Ossó et al.* (2018), as it is defined in section B in the appendix.

The correlation between the dipole index introduced by *Ossó et al.* (2018) and the SEA index shows a significant value of -0.23 for the period from 300-400, but no correlation (-0.03) for the period from 65-135. Furthermore, the correlation of the SST dipole to the ENSO index of the following winter shows a similar behaviour (0.24 for 300-400 and -0.04 for 65-135). Calculating the correlation between this index and the SEA index

for 51 years running windows emphasizes these findings (Figure A.11 in the appendix): The correlation between the SEA and the spring-SST-dipole index seems to be related to the correlation of SEA and PCD index (correlation -0.37) and to the correlation of spring-SST and ENSO (-0.36).

It is apparent that the epoch between year 300 and 400 is outstanding compared to the rest of the model run. Figure 6 shows that is it characterised by the largest PCD-SEA-correlation and the largest amount of variance explained by the SEA. Furthermore, it is also an episode of very strong connection between ENSO and the SEA (red line in Figure A.11 in the appendix) although the correlation between ENSO and the PCD is not exceptionally high (black line in Figure A.11). This section reveals a significant correlation of strong spring SST anomalies in the North Atlantic and the SEA pattern. The cyan and magenta line in Figure A.11 also show significant correlations between the spring SST and the ENSO and SEA index in that epoch. There is no other episode when all these indices reach significant values at the same time.

4 Discussion

In this thesis, the representation of the Summer East Atlantic (SEA) pattern, defined as the third Empirical Orthogonal Function (EOF) of summer (JJA) 500hPa geopotential height over the North Atlantic European (NAE) region (in this dataset; it is the second EOF in ERA-Interim reanalysis data), was analysed in a model run of 700 years. In general, it was found that the SEA pattern is present in a similar way to what was found before by *Wulff et al.* (2017) based on reanalysis data. Characterised by a dipole anomaly between the North Atlantic and the Baltic Sea, it was related to significantly enhanced temperature anomalies in Europe and the surrounding oceans when in its positive state. Simultaneously, enhanced precipitation was found over the North Atlantic, Britain and Scandinavia and reduced precipitation over eastern Europe. Although these results are very similar to the findings of *Wulff et al.* (2017), it is apparent that compared to their study based on ERA-Interim reanalysis data, the results of this model were less clear, with reduced amplitude and spatial extent of the signal. This is the case for the SEA pattern itself that was found to be the third EOF in summer instead of the second and contributes less variance in the model (11.7%) than in ERA (18.7%), but also for the influence on European climate.

In *Wulff et al.* (2017) it was also shown that the SEA pattern is sensitive to tropical forcing, driven by diabatic heating anomalies in the tropical regions of the Pacific and Caribbean that generate Rossby waves propagating towards the North Atlantic. This tropical connection is confirmed in the model data as a precipitation dipole over the tropical Pacific and Caribbean was clearly connected to the SEA pattern. However, these results were found to be weaker than in *Wulff et al.* (2017): The tropical precipitation signal was of lower amplitude compared to that in ERA data, and the dipole in surface air temperature (SAT) and sea surface temperature (SST) that was found to be clearly related to the SEA pattern in the study of *Wulff et al.* (2017), was not significantly present in the analysis of this thesis. The correlation between the Pacific Caribbean Dipole (PCD) index and the SEA index was found to be reduced as well (0.17 compared to 0.56 in ERA), but still statistically significant.

By dividing the 700-year-model run into smaller intervals of 51 years and analyzing the mechanisms within these periods, it was found that both the overall weakening of the SEA pattern and the overall weakening of the tropical forcing, are the result of non-stationarity. The variance explained by the SEA pattern is varying in the model run between 8% and 16% and the correlation between the SEA index and the PCD index is varying between negative values (-0.1) and 0.6. By doing Principal Component analysis for smaller parts of the model run it was found that the SEA pattern was sometimes present as the second or third mode of interannual variance, similar to the ERA-Interim

period, but there are also epochs when no similar pattern is visible in the five most dominant modes. This suggests that the pattern itself lacks robustness. The resulting properties of the SEA pattern as the third EOF, explaining 11.7% of the variance in the North Atlantic and correlated to the PCD at 0.17 are a reasonable consequence of this lack of robustness.

Although the SEA pattern, its impact on European climate and its tropical forcing are all varying, their variations are not necessarily correlated to one another. Most of the time, all three variations seem to be quite independent, especially when the values are more moderate. There are epochs, however, when common features are apparent: The years between 65 and 135 are a good example for a time when the SEA pattern explains little interannual variance and is not related to intense tropical forcing. The other extreme can be found between 300 and 400 when the pattern explains a high amount of interannual variance and is highly influenced by the tropics. This suggests that the results of ERA-Interim data found by *Wulff et al.* (2017) that covers only 40 years only represent a current state of the Earth system, comparable to one of the periods of high correlation of the model run like the one between 300 and 400. However, the finding of the nonstationarity of tropical-extratropical teleconnections is not entirely new. *Lee and Ha* (2015) found a change in the tropical-extratropical teleconnection of circulation patterns associated with El Niño Southern Oscillation (ENSO) and the Asian summer monsoons in the late 1970s and *O'Reilly et al.* (2017) showed varying forecasting skill for the winter Pacific North America pattern and the North Atlantic Oscillation associated with tropical SST forcing.

The analysis of the SEA pattern only for epochs of high correlation (as marked in Figure 6) presents results that are basically similar to what was found for the 700 years, but stronger in amplitude, spatial extent and significance, especially in relation to the tropics, where the SEA pattern was found to be related to strong dipoles of precipitation, SAT and SST. The results of this part of the analysis are very similar to those of *Wulff et al.* (2017) based on the ERA data. For these epochs the pattern is strongly related to tropical convective precipitation anomalies resulting in the generation of Rossby waves. This leads to the conclusion that the recent 40 years covered by the ERA-Interim reanalysis data is one of these periods of high tropical-extratropical teleconnection. In general, this confirms the findings of *Wulff et al.* (2017), but it also gives evidence that there might be other times when the teleconnection is missing. As the mentioned period between year 300 and 400 that is similar to the recent years covered by ERA-Interim data, represents the maximum of explained variance and tropical forcing of the whole model run, it is likely that the SEA pattern's importance in the NAE region and its tropical forcing might decrease in the future.

The analysis of the periods of rather low correlation between the SEA index and PCD index revealed that for a big part of the model run (203 years were selected to represent this low correlation) there is almost no connection between the SEA pattern and the tropical Pacific and Caribbean. Despite this lack of tropical forcing, the pattern was still contributing to interannual variance over the NAE region and able to influence European climate in a similar way, but with reduced amplitude and spatial extent. The SEA pattern can still be present and influence European climate, suggesting that there might be another driving mechanism.

In the study of *Wulff et al.* (2017), it was suggested that the PCD and the SEA pattern were related to the developing ENSO. To analyse this, a period of dominant SEA pattern and high tropical forcing (300-400) was compared to a period of less dominant SEA pattern and effectively no tropical forcing (65-135). It was found that the relation between the PCD and ENSO is very robust, resulting in a constantly produced precipitation dipole anomaly by the developing ENSO. The connection between ENSO and the SEA, however, was found to be varying similar to the PCD-SEA-correlation. This suggests that the influence of the developing ENSO on the SEA pattern is mainly via the precipitation dipole anomalies that are constantly induced by the developing ENSO but do not act as a consistent forcing mechanism for the SEA pattern. The correlation between ENSO and the SEA index does not reach values comparable to the ERA-Interim period (0.47).

By advecting vorticity in the upper troposphere, these precipitation anomalies can act as a source for Rossby waves. By comparing the generation of these Rossby waves for epochs of very strong tropical forcing and effectively no forcing of the SEA pattern, a slightly enhanced Rossby wave source (RWS) is found in the Caribbean region that might explain some of the difference in the tropical forcing. However, the PCD and the SEA pattern are still related to positive RWS in epochs of effectively no tropical forcing. At this point, it has to be stated that the Rossby wave source was calculated by using seasonal means. Previous studies suggested to calculate the RWS for daily data before averaging seasonally, because short-term covariances are an important driver of the Rossby wave generation. Due to the model output being restricted to monthly data, this was not done in this study, but might give a clearer insight into the difference in Rossby wave generation. However, it can be expected that the trend of enhanced Rossby wave source during high correlation periods that was already visible in this study will be further emphasized. The propagation of these Rossby waves seems to be rather similar in low- and high-correlation periods, suggesting that a difference in the upper-tropospheric mean circulation does not contribute to the lack of robustness of the SEA pattern. It is also visible that the main region of the generation of Rossby waves which is the Caribbean (Figure 12) is effected by easterly mean flow (indicated by the black filling in Figure 11)

33

which strongly repels Rossby waves. This apparent contradiction further complicates the interpretation of how the generation and propagation of Rossby waves contributes to the difference in tropical forcing of the SEA pattern.

Another point of this study was the contribution of the spring SST on the SEA pattern that was mentioned before in other studies (*Wulff et al.*, 2017; *Ossó et al.*, 2018; *Cassou et al.*, 2005; *Duchez et al.*, 2016). Anomalies in spring (March/April) SST can be related to the SEA pattern in the model during some episodes of high correlation between the SEA and PCD. Furthermore, the correlation between the dipole SST index introduced by *Ossó et al.* (2018) and the SEA index is correlated to the correlation of the PCD and SEA index at -0.37 which is statistically significant. In periods of high SEA-PCD-correlation, this SST index was found to be correlated not only to the SEA index, but also to the developing ENSO. It is important to note here that the SEA pattern as it was described in *Ossó et al.* (2018) does not necessarily resemble the SEA pattern as defined in *Wulff et al.* (2017) and this analysis. Still, a connection between anomalies in the spring SST and the SEA pattern is indisputable. For future analysis it might be reasonable to introduce another SST index that captures the spring SST response related to the SEA pattern as defined in this study better. As the resources of this thesis are limited, no further investigation was done on the mechanisms responsible for the temporal coincidences of the forcing via tropical diabatic heating associated with the PCD and the forcing via spring SST anomalies in the North Atlantic. However, it is obvious that a connection between both forcing mechanisms and ENSO is present. A further investigation on this topic remains a future task. It is necessary to state here, that the MPI-ESM model used in this study is affected by the North Atlantic cold bias, associated with a misplacement of the Gulf Stream and the North Atlantic Current (*Jungclaus et al.*, 2013). This could result in a shift of the SST anomalies in the model compared to the real world.

This analysis emphasizes the need of model data to analyze long-term developments as reliable observational data is limited and therefore often only represents the current state of the Earth system. It was shown before in other studies that especially tropical-extratropical teleconnections are highly variable on longer time scales (*Lee and Ha*, 2015; *O'Reilly et al.*, 2017). It is also possible that the nature of tropical-extratropical teleconnections can be altered in the future, as was shown by *Lee et al.* (2014) by considering a realistic scenario for the future development of greenhouse gas emissions. This suggests that the results of this analysis may be useful in general, but an analysis on their robustness under different scenarios of enhanced greenhouse gas forcing can provide further valuable results.

5 Conclusion

This thesis provided evidence for the presence of the Summer East Atlantic pattern in a model run of 700 years. As the third most dominant mode of interannual variance, it has high impact on temperatures and precipitation over Europe, but is also related to tropical activity. However, high nonstationarity was found for the SEA pattern itself, but also for its explained variance and its tropical forcing. In comparison to a previous study conducted by *Wulff et al.* (2017) this suggests that the last 40 years represent the current state of the Earth system that is highly similar to a period of high SEA impact and high tropical forcing as it was found in the model run. The presence of other periods in the model run, with very low SEA impact and effectively no relation to the tropics, indicates that this current state might vary in the future, resulting in a SEA pattern of lower dominance and no tropical forcing. Future studies could investigate the drivers of this nonstationarity and a possibly different development under the influence of global warming and the climate change.

References

Cassou, C., L. Terray, and A. S. Phillips, Tropical atlantic influence on european heat waves, *Journal of Climate*, *18*(15), 2805–2811, 2005.

Coumou, D., and S. Rahmstorf, A decade of weather extremes, *Nature Climate Change*, *2*(7), 2012.

Dawson, A., A. J. Matthews, and D. P. Stevens, Rossby wave dynamics of the north pacific extra-tropical response to el niño: importance of the basic state in coupled gcms, *Climate Dynamics*, *37*(1-2), 391–405, 2011.

Dee, D. P., et al., The era-interim reanalysis: configuration and performance of the data assimilation system, *Quarterly Journal of the Royal Meteorological Society*, *137*(656), 553–597, 2011.

Ding, Q., B. Wang, J. M. Wallace, and G. Branstator, Tropical-extratropical teleconnections in boreal summer: Observed interannual variability, *Journal of Climate*, *24*(7), 1878–1896, 2011.

Dommenget, D., and M. Latif, A cautionary note on the interpretation of eofs, *Journal of Climate*, *15*(2), 216–225, 2002.

Duchez, A., et al., Drivers of exceptionally cold north atlantic ocean temperatures and their link to the 2015 european heat wave, *Environmental Research Letters*, *11*(7), 2016.

Dunstone, N., D. Smith, A. Scaife, L. Hermanson, R. Eade, N. Robinson, M. Andrews, and J. Knight, Skilful predictions of the winter north atlantic oscillation one year ahead, *Nature Geoscience*, *9*, 809–814, 2016.

Folland, C. K., J. Knight, H. W. Linderholm, D. Fereday, S. Ineson, and J. W. Hurrell, The summer north atlantic oscillation: Past, present, and future, *Journal of Climate*, *22*(5), 1082–1103, 2009.

Giorgetta, M. A., et al., Climate and carbon cycle changes from 1850 to 2100 in mpi-esm simulations for the coupled model intercomparison project phase 5, *Journal of Advances in Modeling Earth Systems*, *5*(3), 572–597, 2013.

Gollan, G., and R. J. Greatbatch, On the extratropical influence of variations of the upper-tropospheric equatorial zonal-mean zonal wind during boreal winter, *Journal of Climate*, *28*(1), 168–185, 2015.

Greatbatch, R. J., The north atlantic oscillation, *Stochastic Environmental Research and Risk Assessment*, *14*(4), 213–242, 2000.

Greatbatch, R. J., and P.-p. Rong, Discrepancies between different northern hemisphere summer atmospheric data products, *Journal of Climate*, *19*(7), 1261–1273, 2006.

Greatbatch, R. J., H. Lin, J. Lu, K. A. Peterson, and J. Derome, Tropical/extratropical forcing of the ao/nao: A corrigendum, *Geophysical Research Letters*, *30*(14), 2003.

Greatbatch, R. J., G. Gollan, T. Jung, and T. Kunz, Tropical origin of the severe european winter of 1962/1963, *Quarterly Journal of the Royal Meteorological Society*, *141*(686), 153–165, 2012.

Hoskins, B. J., and T. Ambrizzi, Rossby wave propagation on a realistic longitudinally varying flow, *Journal of the Atmospheric Sciences*, *50*(12), 1661–1671, 1993.

Hurrell, J. W., and C. Deser, North atlantic climate variability: The role of the north atlantic oscillation, *Journal of Marine Systems*, *79*, 231–244, 2010.

Hurrell, J. W., Y. Kuchnir, G. Ottersen, and M. Visbeck, *The North Atlantic Oscillation: Climatic Significance and Environmental Impact*, *Geophysical Monograph*, vol. 134, American Geophysical Union, 2003.

Iglesias, I., M. N. Lorenzo, and J. J. Taboada, Seasonal predictability of the east atlantic pattern from sea surface temperatures, *PLOS ONE*, *9*, 1–8, 2014.

Ilyina, T., K. D. Six, J. Segschneider, E. Maier-Reimer, H. Li, and I. Núñez-Riboni, Global ocean biogeochemistry model hamocc: Model architecture and performance as component of the mpi-earth system model in different cmip5 experimental realizations, *Journal of Advances in Modeling Earth Systems*, *5*(2), 287–315, 2013.

Jungclaus, J. H., N. Fischer, H. Haak, K. Lohmann, J. Marotzke, D. Matei, U. Mikolajewicz, D. Notz, and J. S. Storch, Characteristics of the ocean simulations in the max planck institute ocean model (mpiom) the ocean component of the mpi-earth system model, *Journal of Advances in Modeling Earth Systems*, *5*(2), 422–446, 2013.

Lee, J.-Y., and K.-J. Ha, Understanding of interdecadal changes in variability and predictability of the northern hemisphere summer tropical-extratropical teleconnection, *Journal of Climate*, *28*(21), 8634–8647, 2015.

Lee, J.-Y., B. Wang, K.-H. Seo, J.-S. Kug, Y.-S. Choi, Y. Kosaka, K.-J. Ha, H. Kyong, and S. , Future change of northern hemisphere summer tropical-extratropical teleconnection in cmip5 models*, *Journal of Climate*, *27*, 3643–3664, 2014.

Lin, H., Global extratropical response to diabatic heating variability of the asian summer monsoon, *Journal of the Atmospheric Sciences*, *66*, 2697–2713, 2009.

Linderholm, H. W., and C. K. Folland, Summer north atlantic oscillation (snao) variability on decadal to palaeoclimate time scales, *Past Global Changes Magazine*, *25*(1), 57–60, 2017.

North, G. R., T. L. Bell, R. F. Cahalan, and F. J. Moeng, Sampling errors in the estimation of empirical orthogonal functions, *Monthly Weather Review*, *110*(7), 699–706, 1982.

O'Reilly, C. H., J. Heatley, D. MacLeod, A. Weisheimer, T. N. Palmer, N. Schaller, and T. Woollings, Variability in seasonal forecast skill of northern hemisphere winters over the twentieth century, *Geophysical Research Letters*, *44*(11), 5729–5738, 2017.

Ossó, A., R. Sutton, L. Shaffrey, and B. Dong, Observational evidence of european summer weather patterns predictable from spring, *Proceedings of the National Academy of Sciences*, *115*(1), 59–63, 2018.

Reick, C. H., T. Raddatz, V. Brovkin, and V. Gayler, Representation of natural and anthropogenic land cover change in mpi-esm, *Journal of Advances in Modeling Earth Systems*, *5*(3), 459–482, 2013.

Sardeshmukh, P. D., and B. J. Hoskins, The generation of global rotational flow by steady idealized tropical divergence, *Journal of the Atmospheric Sciences*, *45*(7), 1228–1251, 1988.

Scaife, A. A., et al., Skillful long-range prediction of european and north american winters, *Geophysical Research Letters*, *41*(7), 2514–2519, 2014.

Scaife, A. A., et al., Tropical rainfall, rossby waves and regional winter climate predictions, *Quarterly Journal of the Royal Meteorological Society*, *143*(702), 1–11, 2017.

Shimizu, M. H., and I. F. de Albuquerque Cavalcanti, Variability patterns of rossby wave source, *Climate Dynamics*, *37*(3-4), 441–454, 2011.

Stevens, B., et al., Atmospheric component of the mpi-m earth system model: Echam6, *Journal of Advances in Modeling Earth Systems*, *5*(2), 146–172, 2013.

Taylor, K. E., R. J. Stouffer, and G. A. Meehl, An overview of cmip5 and the experiment design, *Bulletin of the American Meteorological Society*, *93*(4), 485–498, 2012.

Trenberth, K. E., G. W. Branstator, D. Karoly, A. Kumar, N.-C. Lau, and C. Ropelewski, Progress during toga in understanding and modeling global teleconnections associated with tropical sea surface temperatures, *Journal of Geophysical Research: Oceans*, *103*(C7), 14,291–14,324, 1998.

von Storch, H., and F. W. Zwiers, *Statistical Analysis in Climate Research*, Cambridge University Press, 1999.

Wang, B., J. Liu, H.-J. Kim, P. J. Webster, S.-Y. Yim, and B. Xiang, Northern hemisphere summer monsoon intensified by mega-el niño/southern oscillation and atlantic multidecadal oscillation, *Proceedings of the National Academy of Sciences*, *110*(14), 5347–5352, 2013.

Wu, Z., and P. Zhang, Interdecadal variability of the mega-enso–nao synchronization in winter, *Climate Dynamics*, *45*(3), 1117–1128, 2015.

Wulff, C. O., R. J. Greatbatch, D. I. V. Domeisen, G. Gollan, and F. Hansen, Tropical forcing of the summer east atlantic pattern, *Geophysical Research Letters*, *44*(21), 11,166–11,173, 2017.

Wulff, O., Personal communication, 2018.

Yu, B., and H. Lin, Tropical atmospheric forcing of the wintertime north atlantic oscillation, *Journal of Climate*, *29*(5), 1755–1772, 2016.

Appendices

A Supporting Figures
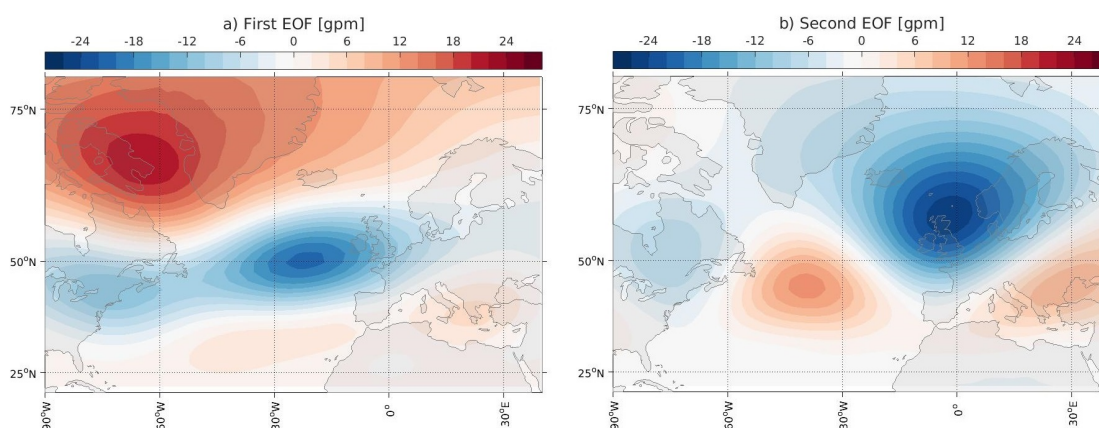
Figure A.1: The first two EOFs of summer (JJA) geopotential height at the 500hPa-level over the North Atlantic European region [90°W - 40°E, 20°N - 80°N]. The first EOF explains 16.8% and the second EOF 14.5% of the interannual variance over the area.
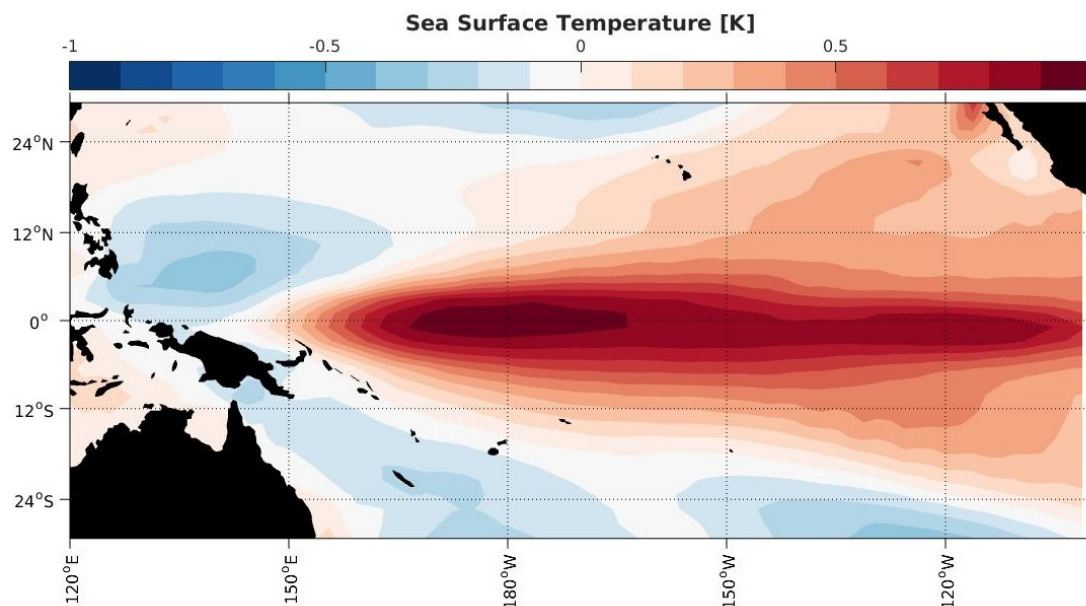
Figure A.2: El Niño Southern Oscillation (ENSO) defined as the first EOF of boreal winter (NDJFM) sea surface temperature in the tropical Pacific. The EOF explains 48.4% of the interannual variance in the area. The corresponding PC time series is used as an index for ENSO in the study.
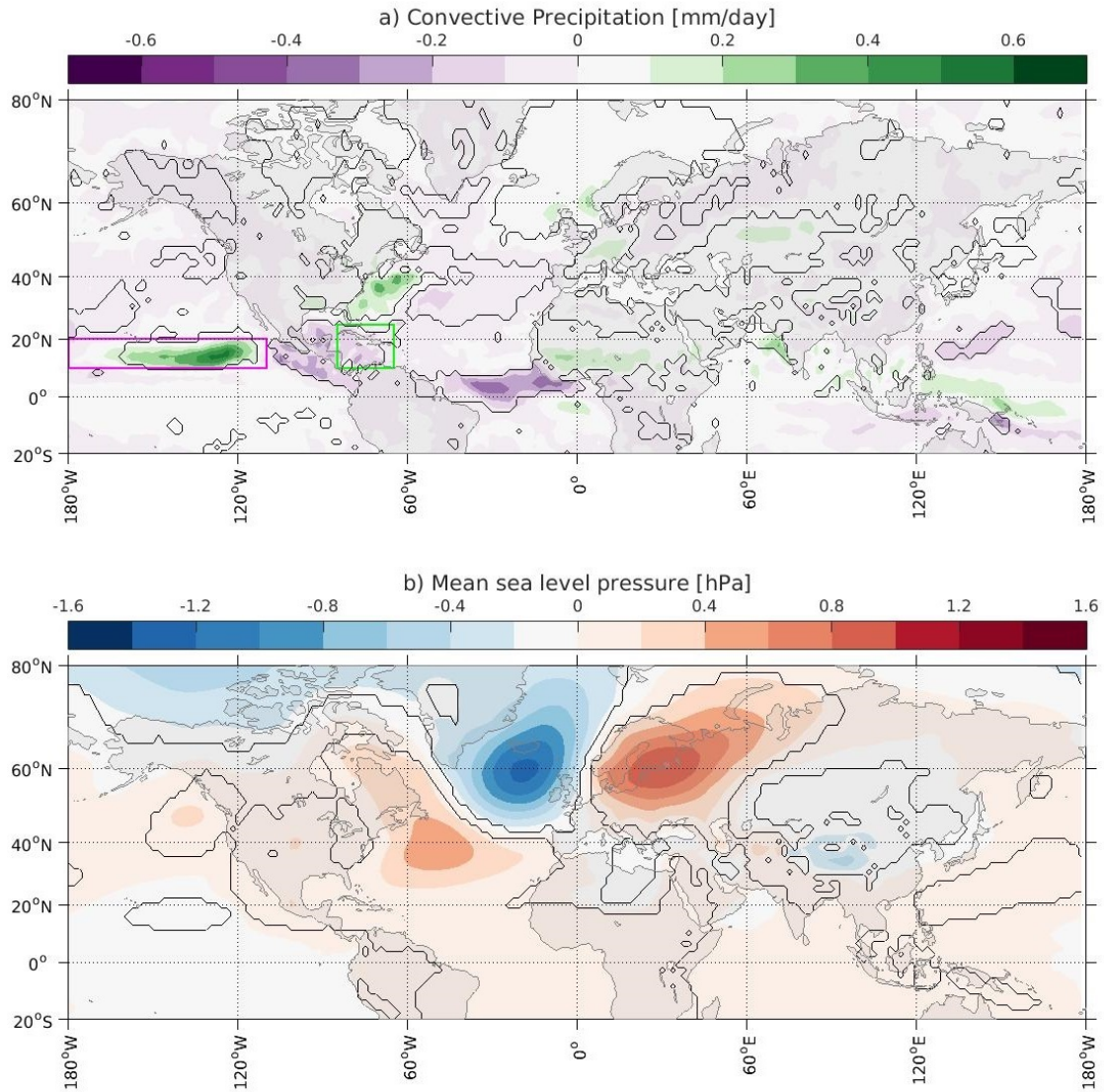
Figure A.3: Regression of a) convective precipitation and b) mean sea level pressure anomalies on the SEA index for the whole 700 years of model output. The solid lines indicate statistic significance at the 95%-level due to a student's t test.
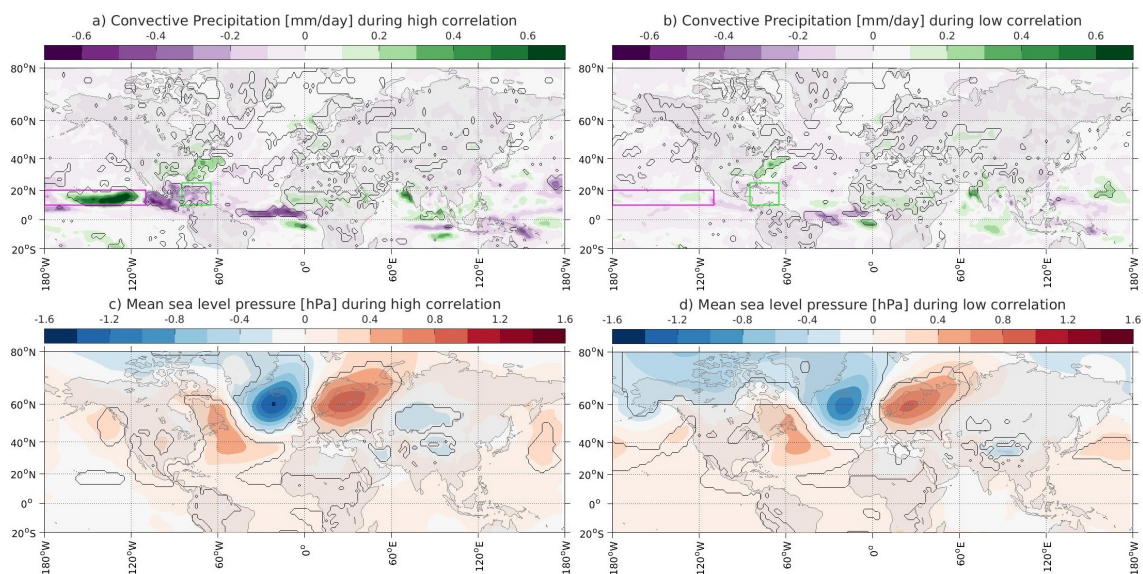
Figure A.4: Regression of a), b) convective precipitation and c), d) mean sea level pressure anomalies on the SEA index for the years of a), c) high correlation and b), d) low correlation. The years of high (low) correlation are marked by the green (grey) filling in Figure 6. The solid lines indicate statistic significance at the 95%-level due to a student's t test.
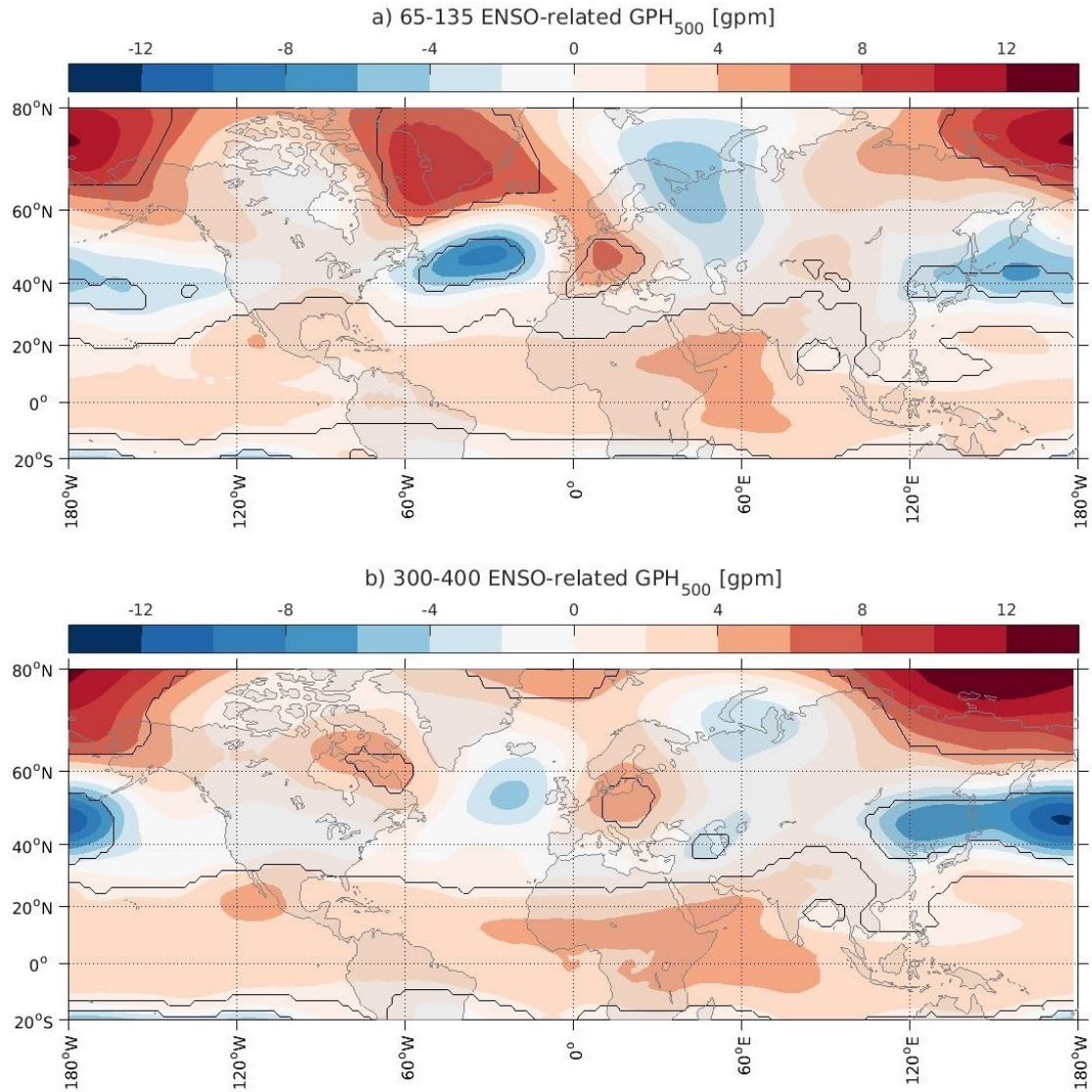
Figure A.5: Regression of preceding summer (JJA) anomalies of 500hPa geopotential height on the NDJFM ENSO index for the time period between a) 65-135 and b) 300-400. The solid lines indicate statistic significance at the 95%-level due to a student's t test.
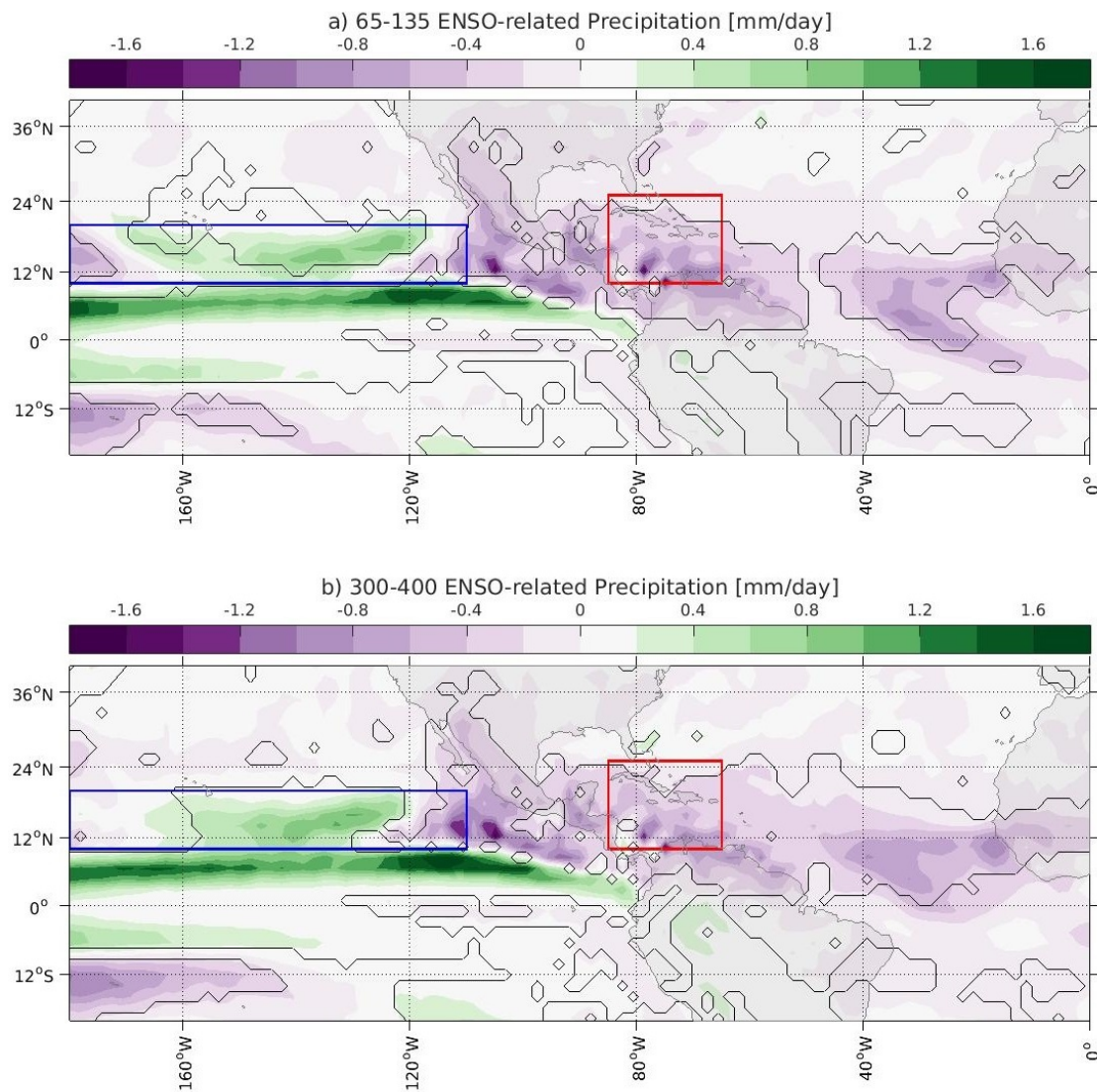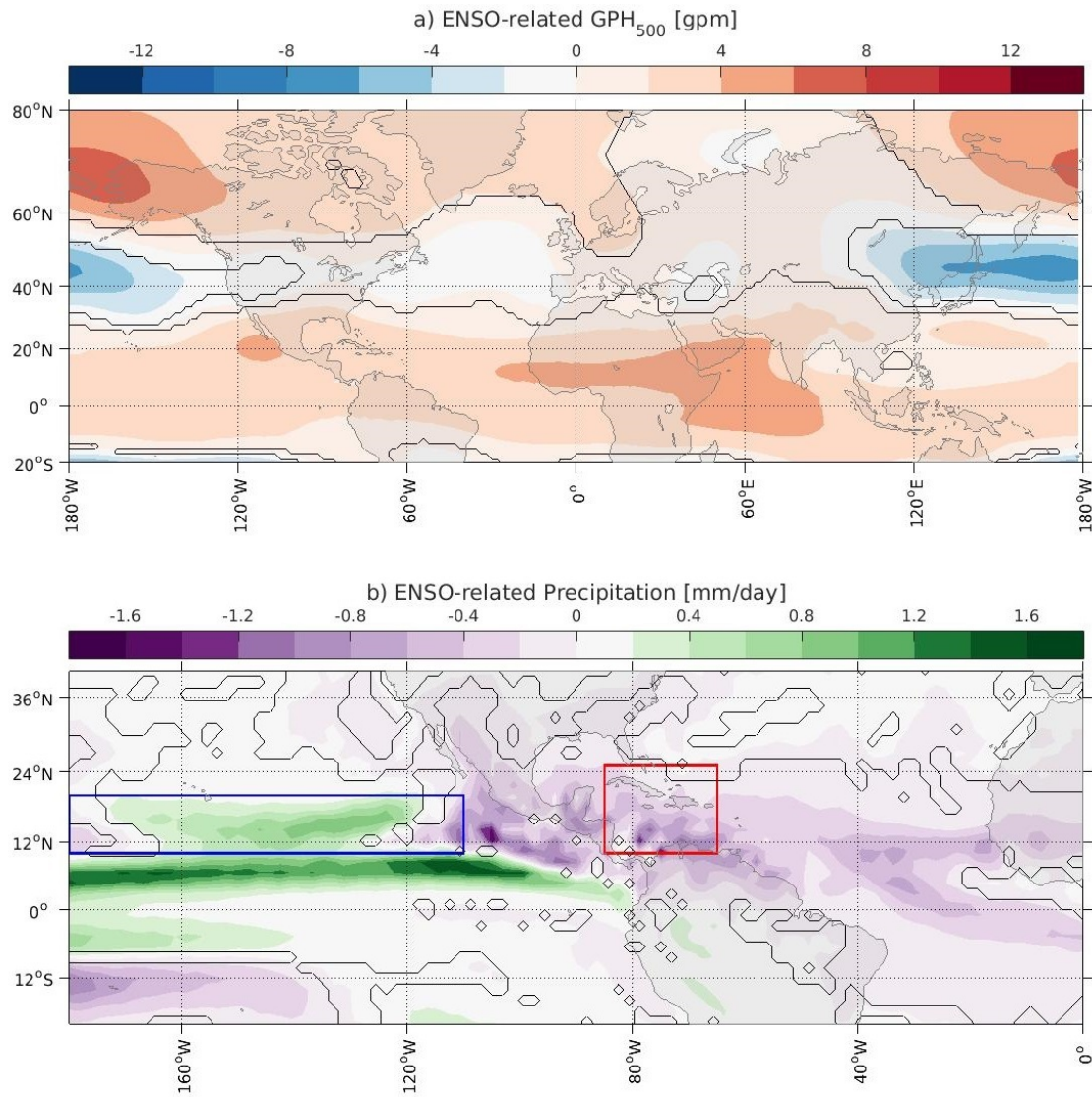
Figure A.6: Regression of preceding summer (JJA) precipitation anomalies on the ND-JFM ENSO index for the time period between a) 65-135 and b) 300-400. The solid lines indicate statistic significance at the 95%-level due to a student's t test.

Figure A.7: Regression of preceding summer (JJA) a) GPH$_{500}$ anomalies and b) precipitation anomalies on the NDJFM ENSO index for the whole 700 years of model output. The solid lines indicate statistic significance at the 95%-level due to a student's t test.
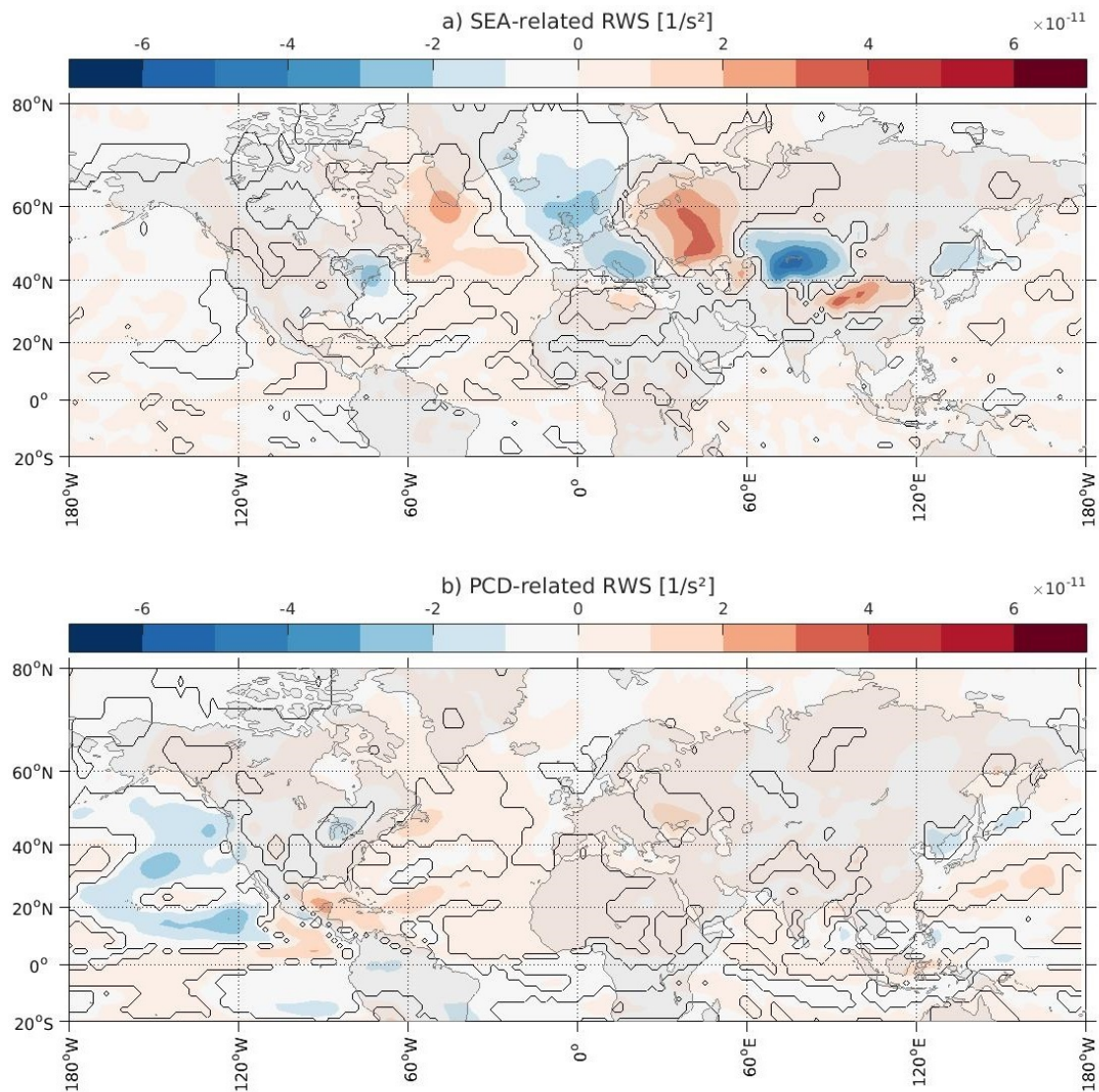
Figure A.8: Rossby wave source regressed on the a) SEA index and b) PCD index for the whole 700 years of model output. The RWS is calculated from seasonal means (JJA). The solid lines indicate statistic significance at the 95%-level due to a student's t test.
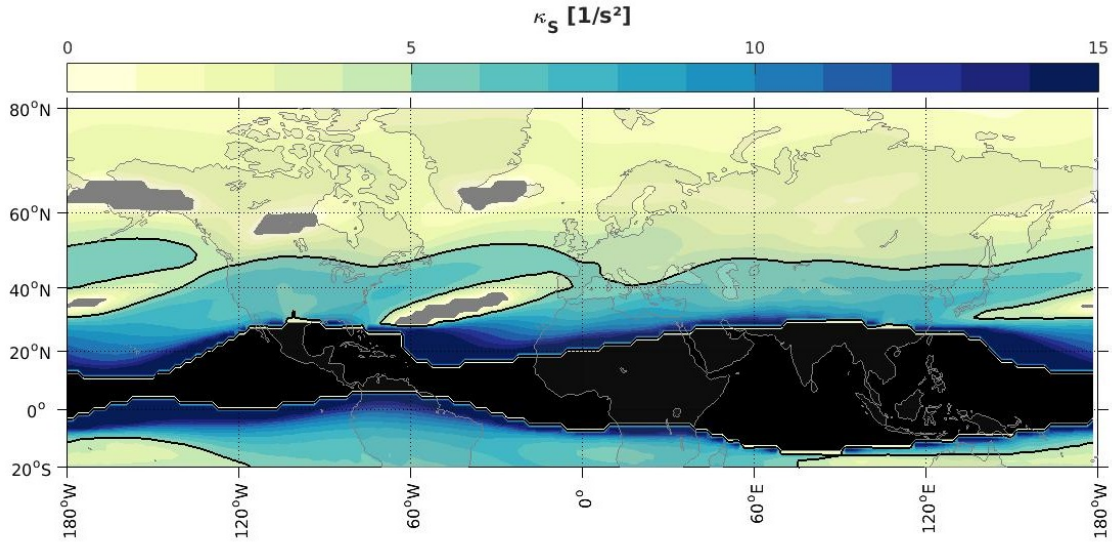
Figure A.9: Stationary zonal Rossby wavenumber, calculated from seasonal means (JJA) of the flow field. Averaged over the whole 700 years of model output.
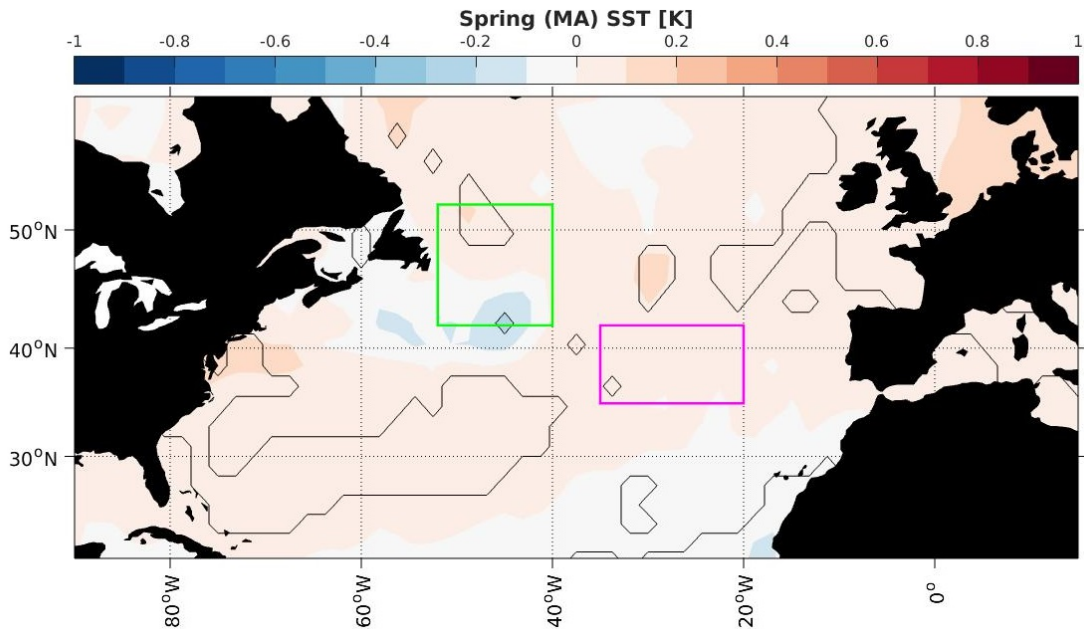

Figure A.10: Spring (March/ April) SST regressed on the SEA index of the following summer (JJA) for the whole 700 years of model output. The solid lines indicate statistic significance at the 95%-level due to a student's t test. The boxes refer to the regions for the calculation of the SST index following *Ossó et al.* (2018) as defined in section B.

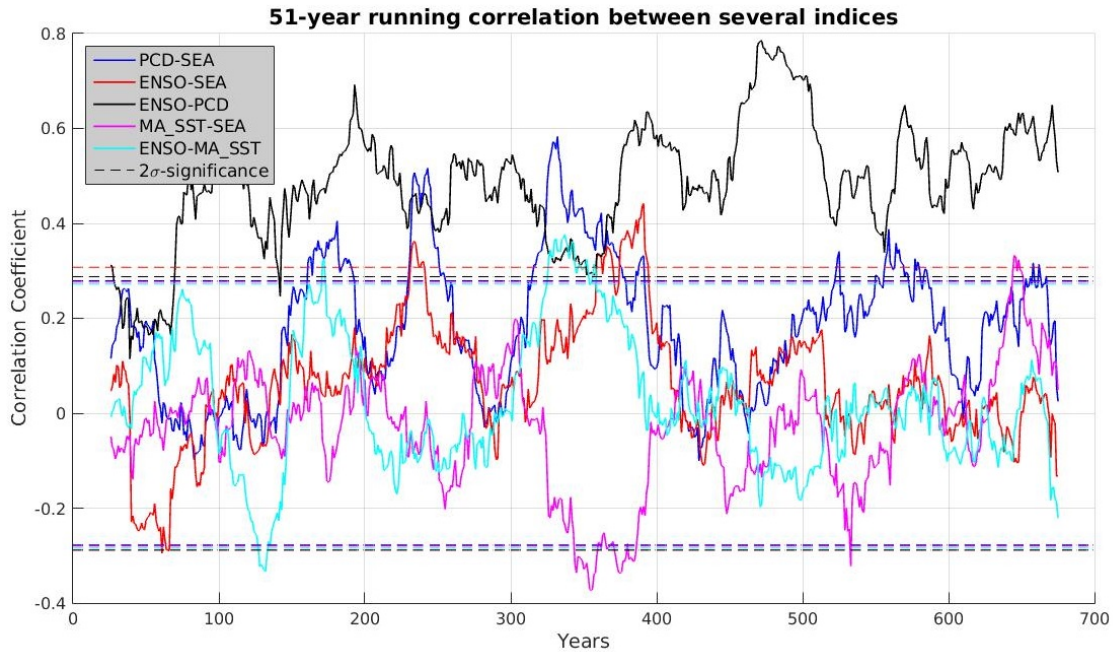Figure A.11: Running correlations of 51-year-windows of different indices used in the study. The dashed lines show the 2σ-significance level.
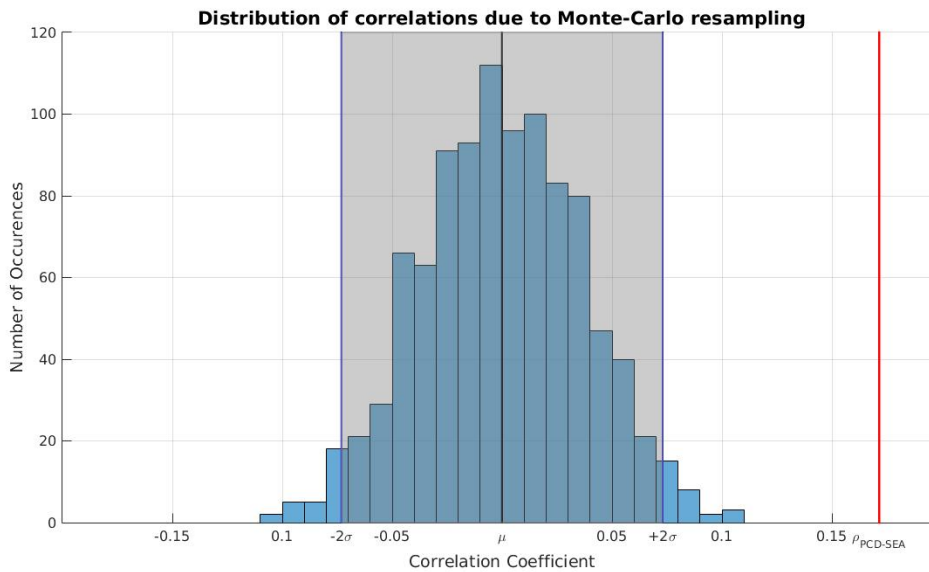

Figure A.12: Example for the distribution of random correlations between the PCD and SEA index due to the Monte Carlo resampling technique. The distribution consists of 1000 correlations between 700 random years of PCD index and SEA index. The black line indicates the mean μ of these correlations and the blue lines two standard deviations (-2σ, $+2\sigma$). The shaded area between these blue lines covers all values within two standard deviations from the mean which coincides with 95% of the values for normal distributions. The red line indicates the real correlation between the SEA index and the PCD index in the 700-year lasting model run ($\rho_{PCD-SEA}$). As this is 0.17, it exceeds the shaded area and the 95%-level and is therefore considered significant.

B   Definition of the indices

Different indices were used throughout the study. This section gives an overview over the different indices and their exact definitions.

- **SEA index:** The Summer East Atlantic (SEA) index is used as a measure of the SEA pattern. It is defined as the corresponding PC time series to the third EOF of summer (JJA) geopotential height at the 500hPa-level over the North Atlantic European region [90°W - 40°E; 20°N - 80°N] over the whole 700 years of the model run. The corresponding pattern can be found in Figure 3.

- **PCD index:** The Pacific Caribbean Dipole (PCD) index expresses the strength of the Pacific Caribbean precipitation Dipole. For this purpose, the area average of normalized precipitation anomalies in a tropical Pacific region [180°W - 110°W; 10°N - 20°N] and the area average of normalized precipitation anomalies in a Caribbean region [85°W - 65°W; 10°N - 25°N] are calculated. The boxes can be seen in Figure 4. The PCD index is then defined as the normalized difference of the Pacific average minus the Caribbean average. In this study, summer (JJA) seasonal means of precipitation are used to calculate the index for every year.

- **ENSO index:** As a measure for the strength of El Niño Southern Oscillation (ENSO) this index is defined as the corresponding PC time series to the first EOF of boreal winter (NDJFM) sea surface temperature in the tropical Pacific [120°E - 100°W; 30°S - 30°N]. The corresponding pattern resembles El Niño well and can be found in Figure A.2. The resulting index is well correlated to the Niño 3.4 index at 0.92.

- **Niño 3.4 index:** The Niño 3.4 index is defined as the area average of sea surface temperature over the Niño 3.4 region which is located in the tropical Pacific [120°W - 170°W; 5°S - 5°N]. For comparison the index was calculated by using NDJFM means in this study.

- **Spring SST index:** In this study, a spring sea surface temperature (SST) index that was introduced by *Ossó et al.* (2018) was used as a measure of spring sea surface temperature anomalies over the North Atlantic. It is defined as a dipole index over the area averages of sea surface temperature in spring (MA) in a north western box [42°N - 52°N; 52°W - 40°W] minus a south eastern box [35°N - 42°N; 35°W - 20°W]. The location of the boxes can be seen in Figure 13. Both area averages and the resulting index are normalized.

C Student's t test values

By calculating the signifcance via the student's t test it is necessary to make use of the significance threshold value t. This value is dependent of the desired confidence level and the degrees of freedom of a sample size. All significance tests in this study were conducted on the 95%-significance level, but for different sample sizes. The values of t that were used for the different sample sizes can be found in the following table.

Sample Size	t
39	2.042
51	2.021
71	2.009
101	1.984
166	1.976
203	1.972
700	1.96

It has to be stated here that the number of degrees of freedom is usually different from the sample size as two following values are often not independent from one another. However, the real number of degrees of freedom is hard to estimate and the values of t used here is only an estimation that might be wrong. It was shown that slight changes of the values of t do not have big impacts on the results.

D List of abbreviations

AGCM	atmospheric general circulation model
CGT	circumglobal teleconnection
CMAP	CPC Merged Analysis of Precipitation
CMIP5	Couple Model Intercomparison Project phase 5
ECMWF	European Centre for Medium-Range Weather Forecasts
ENSO	El Niño Southern Oscillation
EOF	Empirical Orthogonal Function
GCM	general circulation model
GPH	geopotential height
GPH_{500}	500hPa-level of GPH
ISM	Indian summer monsoon
MPI-ESM	Max-Planck-Institute Earth System Model
MSLP	mean sea level pressure
NAE	North Atlantic European
NAO	North Atlantic Oscillation
NH	northern hemisphere
PC	Principal Component
PCA	Principal Component analysis
PCD	Pacific Caribbean Dipole
RWS	Rossby wave source
SAT	surface air temperature
SCRIP	spherical coordinate remapping and interpolation package
SEA	Summer East Atlantic
SNAO	Summer North Atlantic Oscillation
SST	sea surface temperature
WNPSM	Western North Pacific summer monsoon

Erklärung

Hiermit erkläre ich, dass ich die vorliegende Arbeit selbständig und ohne fremde Hilfe angefertigt und keine anderen als die angegebenen Quellen und Hilfsmittel verwendet habe.

Die eingereichte schriftliche Fassung der Arbeit entspricht der auf dem elektronischen Speichermedium.

Weiterhin versichere ich, dass diese Arbeit noch nicht als Abschlussarbeit an anderer Stelle vorgelegen hat.

Kiel, 12.12.2018